Monthly Notices
of the
ROYAL ASTRONOMICAL SOCIETY

MNRAS **507,** 5991–6011 (2021)
Advance Access publication 2021 September 7

https://doi.org/10.1093/mnras/stab2374

NGTS clusters survey – III. A low-mass eclipsing binary in the Blanco 1 open cluster spanning the fully convective boundary

Gareth D. Smith,[1★] Edward Gillen,[2,1†] Didier Queloz,[1] Lynne A. Hillenbrand,[3] Jack S. Acton,[4] Douglas R. Alves,[5] David R. Anderson,[6,7] Daniel Bayliss,[6,7] Joshua T. Briegal,[1] Matthew R. Burleigh,[4] Sarah L. Casewell,[4] Laetitia Delrez,[8,9] Georgina Dransfield,[10] Elsa Ducrot,[9] Samuel Gill,[6,7] Michaël Gillon,[9] Michael R. Goad,[4] Maximilian N. Günther,[11‡] Beth A. Henderson,[4] James S. Jenkins,[5,12] Emmanuël Jehin,[8] Maximiliano Moyano,[13] Catriona A. Murray,[1] Peter P. Pedersen,[1] Daniel Sebastian,[10] Samantha Thompson,[1] Rosanna H. Tilbrook,[4] Amaury H. M. J. Triaud,[10] Jose I. Vines[5] and Peter J. Wheatley[6,7]

[1]*Astrophysics Group, Cavendish Laboratory, J. J. Thomson Avenue, Cambridge CB3 0HE, UK*
[2]*Astronomy Unit, Queen Mary University of London, Mile End Road, London E1 4NS, UK*
[3]*Department of Astronomy, California Institute of Technology, 1200 East California Boulevard, Pasadena, CA 91125, USA*
[4]*School of Physics and Astronomy, University of Leicester, University Road, Leicester LE1 7RH, UK*
[5]*Departamento de Astronomia, Universidad de Chile, Casilla 36-D, Santiago, Chile*
[6]*Department of Physics, University of Warwick, Gibbet Hill Road, Coventry CV4 7AL, UK*
[7]*Centre for Exoplanets and Habitability, University of Warwick, Gibbet Hill Road, Coventry CV4 7AL, UK*
[8]*Space Sciences, Technologies and Astrophysics Research (STAR) Institute, University of Liège, 19C Allèe du 6 Août, B-4000 Liège, Belgium*
[9]*Astrobiology Research Unit, University of Liège, Allée du 6 Août, 19, B-4000 Liège (Sart-Timan), Belgium*
[10]*School of Physics and Astronomy, University of Birmingham, Edgbaston, Birmingham B15 2TT, UK*
[11]*Department of Physics, and Kavli Institute for Astrophysics and Space Research, Massachusetts Institute of Technology, Cambridge, MA 02139, USA*
[12]*Núcleo de Astronomía, Facultad de Ingeniería y Ciencias, Universidad Diego Portales, Avenida Ejército 441, Santiago, Chile*
[13]*Instituto de Astronomía, Universidad Católica del Norte, Angamos 0610, 1270709 Antofagasta, Chile*

Accepted 2021 August 13. Received 2021 August 13; in original form 2020 July 16

ABSTRACT

We present the discovery and characterization of an eclipsing binary identified by the Next Generation Transit Survey in the ∼115-Myr-old Blanco 1 open cluster. NGTS J0002−29 comprises three M dwarfs: a short-period binary and a companion in a wider orbit. This system is the first well-characterized, low-mass eclipsing binary in Blanco 1. With a low mass ratio, a tertiary companion, and binary components that straddle the fully convective boundary, it is an important benchmark system, and one of only two well-characterized, low-mass eclipsing binaries at this age. We simultaneously model light curves from NGTS, *TESS*, SPECULOOS, and SAAO, radial velocities from VLT/UVES and Keck/HIRES, and the system's spectral energy distribution. We find that the binary components travel on circular orbits around their common centre of mass in $P_{\rm orb} = 1.098\,005\,24 \pm 0.000\,000\,38$ d, and have masses $M_{\rm pri} = 0.3978 \pm 0.0033$ M$_\odot$ and $M_{\rm sec} = 0.2245 \pm 0.0018$ M$_\odot$, radii $R_{\rm pri} = 0.4037 \pm 0.0048$ R$_\odot$ and $R_{\rm sec} = 0.2759 \pm 0.0055$ R$_\odot$, and effective temperatures $T_{\rm pri} = 3372\,^{+44}_{-37}$ K and $T_{\rm sec} = 3231\,^{+38}_{-31}$ K. We compare these properties to the predictions of seven stellar evolution models, which typically imply an inflated primary. The system joins a list of 19 well-characterized, low-mass, sub-Gyr, stellar-mass eclipsing binaries, which constitute some of the strongest observational tests of stellar evolution theory at low masses and young ages.

Key words: binaries: eclipsing – binaries: spectroscopic – stars: evolution – stars: fundamental parameters – stars: low mass – open clusters and associations: individual: Blanco 1.

1 INTRODUCTION

Theories of stellar evolution are integral to our understanding of observational astrophysics. By considering the relevant physics and phenomena, e.g. thermodynamics, ionization states, nuclear reaction pathways, radiative transfer, convection, atmospheric opacity, interior-atmosphere boundary conditions, gravitational contraction, rotation, and magnetic fields, such theories can be used to model the temporal evolution of stellar properties (radius, luminosity, and effective temperature) for stars of given mass and metallicity.

Stellar evolution models also play a role in calibrating various astrophysical time-scales and relations, including the initial

★ E-mail: gds38@cam.ac.uk
† Winton Fellow.
‡ Juan Carlos Torres Fellow.

mass function (Hillenbrand, Bauermeister & White 2008; Bastian, Covey & Meyer 2010), the lifetimes of protoplanetary discs (Haisch, Lada & Lada 2001; Ribas et al. 2014), the formation and migration time-scales of giant planets (Bell et al. 2013; Ribas, Bouy & Merín 2015), and the age–activity–rotation relations of stars (Mamajek & Hillenbrand 2008; Meibom et al. 2015). In addition, our knowledge of the true properties and occurrence rates of exoplanets hinges on our knowledge of their host stars, which depends on accurate stellar models (Gaidos & Mann 2013; Burke et al. 2015; Berger et al. 2018). Given the reach of stellar evolution theory, it is essential to critically test model predictions against observation.

Open clusters act as important astrophysical testing grounds for theory, permitting the study of stellar evolution on coeval populations of stars. Detached, double-lined eclipsing binaries (EBs) in open clusters are excellent tools for calibrating evolutionary models, as they allow, through a combination of photometry and spectroscopy, precise determination of masses, radii, luminosities, and temperatures (Andersen 1991; Torres, Andersen & Giménez 2010). In the best cases, such as with space-based photometry, it is possible to measure mass and radius with minimal theoretical assumptions to a precision better than 1 per cent (e.g. Torres et al. 2018; Maxted et al. 2020; Murphy et al. 2020; Southworth 2021). When accompanied by knowledge of cluster metallicity, which may be derived spectroscopically, EB measurements and stellar evolution models can provide age estimates (e.g. David et al. 2019; Gillen et al. 2020a) and valuable comparisons between dating methods such as isochrone fitting, the lithium depletion boundary (LDB), gyrochronology, and asteroseismology (Soderblom 2010; Soderblom et al. 2014).

Discrepancies between observations and model predictions tend to be more common at young ages and low masses, where models have often been found to underpredict stellar radii for a given mass and overpredict effective temperatures (Irwin et al. 2011; von Braun et al. 2012; Torres 2013; Zhou et al. 2015; Dittmann et al. 2017; Triaud et al. 2020). The extent to which these disagreements are due to model inaccuracies versus unaccounted-for systematic uncertainties related to star-spots, the effects of additional stars in the system, or other factors is, however, an active area of discussion (Morales et al. 2010; Windmiller, Orosz & Etzel 2010; Feiden & Chaboyer 2012a; Somers & Pinsonneault 2015).

One explanation for the departure of models from observation is that strong magnetic fields could inhibit the outward flow of energy by suppressing global convection (Mullan & MacDonald 2001) or inducing greater spot coverage (Chabrier, Gallardo & Baraffe 2007). In order to maintain balance between energy released in the core and flux leaving the stellar surface, the star would expand with an accompanying drop in effective temperature. The fact that most well-studied EBs have short orbital periods with synchronized rotational periods means that rapid rotation is likely to drive strong magnetic fields in these systems and hence could contribute to the observed discrepancies. In support of this idea, Kraus et al. (2011) found that EBs with orbital periods $\leq$1 d were elevated in the mass–radius plane. However, in their study of the radius discrepancy in low-mass stars, Spada et al. (2013) found that, although the components of short-orbital period systems are seen to be the most deviant among EBs, those deviations are matched by the single-star sample. Interferometric angular diameter measurements by Boyajian et al. (2012) led to a similar conclusion, indicating that, for a given mass, single and binary star radii are indistinguishable. Mann et al. (2015) found, in their study of 183 nearby K7–M7 single stars, comparable discrepancies with models as found for EBs, suggesting that underlying model assumptions to do with opacity or convective mixing length are more likely to be the root cause. Finally, in their exploration of the radius inflation problem for M dwarfs on the main sequence, Morrell & Naylor (2019) took an all-sky sample of $>$15 000 stars and employed a spectral energy distribution (SED) fitting method, using *Gaia* DR2 distances and multiwave-band photometry, to determine empirical relations between luminosity, temperature, and radius. They found measured radii to be inflated by 3–7 per cent, but, significantly, found that the stars lie on a very tight sequence, with a scatter $<$1–2 per cent. This, along with their finding of no appreciable correlation between observational indicators of magnetic activity and radius inflation, led them to conclude that stellar magnetism cannot currently explain the radius inflation in main-sequence M dwarfs, a conclusion that dovetails with the above-referenced results, suggesting that detached EBs may not be inflated with respect to the single-star population.

The young-age, low-mass region of EB parameter space remains fairly sparsely populated by well-characterized systems, due to the relative scarcity of young, open clusters and the intrinsic faintness of low-mass stars. Therefore, any additional systems with precisely measured parameters represent benchmark tests of current models.

Blanco 1 was discovered in 1949 (Blanco 1949). It is an open cluster situated in the local spiral arm, in the direction towards and below the Galactic Centre. The cluster is home to 489 *Gaia* DR2-confirmed member stars at a distance of $\sim$240 pc (Gaia Collaboration 2018, hereafter G18), ranging from A to M spectral types (Gillen et al. 2020b), with $\sim$40 likely brown dwarf members (Moraux et al. 2007; Casewell et al. 2012). The metallicity of Blanco 1 is slightly supersolar; Ford, Jeffries & Smalley (2005) and Netopil et al. (2016) derive [Fe/H] $= +0.04 \pm 0.04$ and $+0.03 \pm 0.07$, respectively. It has an on-sky stellar density of $\sim$30 stars pc^{-2} (Moraux et al. 2007) and a low reddening along the line of sight [$E(B-V) \sim 0.010$; G18]. Blanco 1 is in many ways like a smaller, less dense version of the Pleiades ($\sim$110 Myr, 1326 *Gaia* DR2 members, on-sky stellar density $\sim$65 stars pc^{-2}, [Fe/H] ~ -0.01; Moraux et al. 2007; G18).

A range of age estimates exists for Blanco 1 from studies made during the past 25 yr: 90 ± 25 Myr based on Hα emission (Panagi & O'dell 1997); 132 ± 24 and 115 ± 10 Myr from the LDB (Cargile, James & Jeffries 2010; Juarez et al. 2014); 146 ± 14 Myr based on gyrochronology (Cargile et al. 2014); and $\sim$100 Myr based on isochrone fitting (Zhang et al. 2020, hereafter Z20). Despite the variance, Blanco 1 is known to be young, and the LDB age of 115 ± 10 Myr (Juarez et al. 2014) was found to be a good fit to the lower main sequence of the *Gaia* DR2-confirmed members. Clusters at this age are simultaneously home to low-mass stars contracting down on to the main sequence, intermediate-mass stars in a steady hydrogen-burning state, and high-mass stars evolving off the main sequence (David et al. 2016), making them all the more suited to investigations of stellar evolution.

The Next Generation Transit Survey (NGTS) survey (Chazelas et al. 2012; Wheatley et al. 2013, 2017; McCormac et al. 2017), located at ESO's Paranal Observatory, Chile, has been operational since early 2016. Its primary goal is the extension of ground-based transit detections of exoplanets to the Neptune size range, e.g. NGTS-4b, a sub-Neptune-sized planet in the 'Neptunian Desert' (West et al. 2019). The enormous amount of data collected by the survey has led to many other interesting discoveries, including the most massive planet orbiting an M-type star NGTS-1b (Bayliss et al. 2018); an ultrashort-period brown dwarf transiting a tidally locked and active M dwarf (Jackman et al. 2019); the most eccentric eclipsing M-dwarf binary system found to date (Acton et al. 2020a); a transiting 'warm Saturn' recovered from a *TESS* (*Transiting Exoplanet Survey Satellite*; Ricker et al. 2015) single-transit event (Gill et al. 2020);

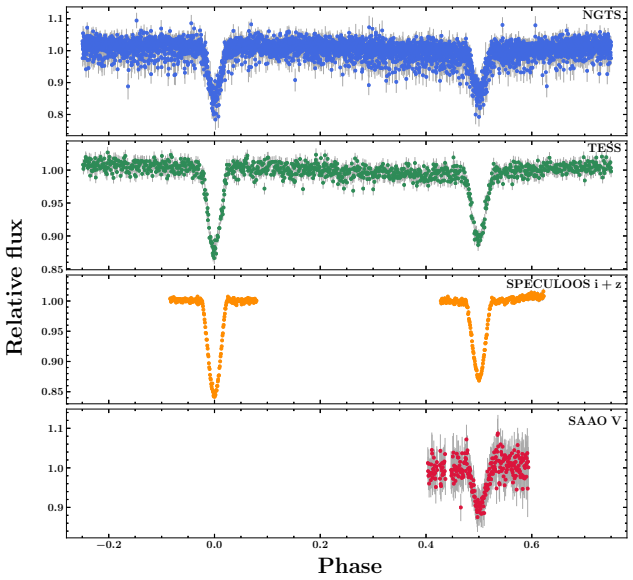

Figure 1. All light curves of NGTS J0002−29, normalized and phase folded on the orbital period. Top to bottom are NGTS, *TESS*, SPECULOOS ($I + z'$ band), and SAAO (V band), respectively.

and transit timing variations on the ∼540-d-period exoplanet, HIP 41378 f (Bryant et al. 2021). NGTS operations include a survey of nearby open clusters and star-forming regions (see Gillen et al. 2020b for Paper I and Jackman et al. 2020 for Paper II), within which the subject of this paper was detected.

We present the identification and characterization of J00024841−2953539 (hereafter NGTS J0002−29) as a triple M-dwarf system in Blanco 1, comprising a short-period EB with a tertiary companion. In Section 2, we describe our observations. We provide details of our modelling procedure in Section 3 and give the results in Section 4. Section 5 presents a discussion, followed by conclusions in Section 6.

2 OBSERVATIONS

NGTS J0002−29 was identified as an EB using NGTS photometry. The on-sky separation from its nearest neighbour in the *Gaia* catalogue – a 21-mag object with no parallax measurement – is 24 arcsec. Objects of comparable brightness are more than 60 arcsec distant. Follow-up photometry was obtained from SPECULOOS-South (Burdanov et al. 2018; Delrez et al. 2018; Gillon 2018; Murray et al. 2020; Sebastian et al. 2021) and the South African Astronomical Observatory (SAAO; Coppejans et al. 2013). It has also been observed by *TESS*. Phase-folded light curves of NGTS J0002−29 are shown in Fig. 1. An initial radial velocity (RV) point was taken with the High-Resolution Echelle Spectrometer (HIRES; Vogt et al. 1994) on the Keck 10-m telescope in Hawaii. Additional spectra were obtained with the Ultraviolet and Visual Echelle Spectrograph (UVES; Dekker et al. 2000), installed on the Very Large Telescope (VLT) in Paranal (Program ID 0103.C-0902; PI Gillen). The astrometric properties and identifiers for the system are listed in Table 1.

2.1 NGTS photometry

The NGTS facility contains an array of twelve 20-cm wide-field robotic telescopes, each with a 2.8° field of view, 5-arcsec pixels, and a 520–890-nm bandpass. The set-up is optimized for observations of K and early M dwarfs. Standard operations, as implemented here, involve 10-s exposures at a cadence of 13 s. Aperture photometry is performed with the CASUTOOLS[1] photometry package. Modified versions of the SysRem (Tamuz, Mazeh & Zucker 2005) and Box-fitting least-squares (Kovács, Zucker & Mazeh 2002) algorithms are used for detrending and transit/eclipse detection. Centroiding, as described in Günther et al. (2017), is integrated into the pipeline as a means of identifying false positives. Full details of the facility and the reduction pipeline can be found in Wheatley et al. (2017).

NGTS J0002−29 was identified as an EB in 2018 September, following an extended observing campaign on the Blanco 1 open cluster (NGTS field NG0004−2950) (Gillen et al. 2020b). NGTS J0002−29 was observed on 135 nights, producing 201 773 images across 196 d from 2017 May 7 to 2017 November 18, including 45 full eclipses (19 primary and 26 secondary) and numerous partial eclipses.

Table 1. Identifiers and astrometric properties for NGTS J0002−29.

Property	Value	Source
Identifier	J00024841−2953539	2MASS
Identifier	2320868389659322368	*Gaia* eDR3
Identifier	TIC 313934158	*TESS*
RA	$00^{h}02^{m}48\overset{s}{.}4549$	*Gaia* eDR3
Dec.	$-29°53'53\overset{''}{.}8898$	*Gaia* eDR3
$\mu_{\rm R.A.}$ (mas yr^{-1})	18.978 ± 0.231	*Gaia* eDR3
$\mu_{\rm Dec.}$ (mas yr^{-1})	3.615 ± 0.203	*Gaia* eDR3
Parallax (mas)	3.7976 ± 0.2555	*Gaia* eDR3
Note	Epoch is J2016.0 for *Gaia* eDR3	

2.2 *TESS* photometry

NGTS J0002−29 (TIC 313934158) was observed by *TESS* in Sector 2 between 2018 August 23 and 2018 September 20 (Camera 1; CCD 2). The *TESS* field of view per camera is 24 × 24 deg (21 arcsec per pixel) and the bandpass runs from 600 to 1000 nm. We extracted our light curve from the 30-min cadence full-frame images using the ELEANOR software package (v1.0.5; Feinstein et al. 2019). The eclipse depths are diluted in the *TESS* light curves due to flux from neighbouring stars, so we tested single-pixel apertures to see how much the effect could be mitigated. In the end, the default two-pixel aperture was selected due to its reduced scatter, because the difference in dilution was minimal and the effect would need to be accounted for in the modelling for any choice of aperture.

2.3 SPECULOOS photometry

We monitored primary and secondary eclipses using the Callisto telescope at the SPECULOOS-South facility,[2] an observatory composed of four semirobotic independent 1-m telescopes, located at ESO Paranal, Chile. Each telescope is equipped with a deep-depletion 2k × 2k CCD detector optimized for the near-infrared, with a 12 × 12 arcmin field of view (0.35 arcsec per pixel). We selected the $I + z'$ filter, which has >90 per cent transmission from 750 to ∼1100 nm and an exposure time of 60 s. Full details of the photometry pipeline can be found in Murray et al. (2020), but in brief, the science images

[1] http://casu.ast.cam.ac.uk/surveys-projects/software-release
[2] https://www.eso.org/public/teles-instr/paranal-observatory/speculoos

are calibrated with standard methods of bias and dark subtraction and flat-field correction, followed by aperture photometry and a differential photometry algorithm, which uses a weighted ensemble of comparison stars to correct for atmospheric and instrumental systematics. The observations took place on the nights of 2018 October 31 and 2018 November 28 for primary and secondary eclipses, respectively.

2.4 SAAO photometry

NGTS J0002−29 was observed by the SAAO 1-m telescope on 2020 November 12. Observations were conducted over ∼4.5 h using the SHOC camera (Coppejans et al. 2013), in the *V* band. The data were bias and flat-field corrected via the standard procedure, using the SAFPHOT[3] PYTHON package. SAFPHOT was also used to perform differential photometry on the target, utilizing the SEP package (Barbary 2016) to extract aperture photometry for both the target and nearby comparison stars. The sky background was measured and subtracted by SEP, using a box size and filter width that minimized the background residuals across the frame after the stars had been masked. A 32-pixel box size and a 2-pixel box filter were found to give the best results. A single bright comparison star was used to perform differential photometry on the target, with a 2.1-pixel-radius aperture, which was found to maximize the signal-to-noise.

2.5 HIRES spectroscopy

In order to confirm its nature as a young low-mass cluster member, and spectrally resolve the binary, the W. M. Keck Observatory Keck I telescope and the high-dispersion spectrograph HIRES (Vogt et al. 1994) were used to acquire the first spectrum of the source. The observation was obtained on 2018 November 11 with the C5 decker, resulting in a spectrum with a resolving power $\mathcal{R} = 36\,000$ over 4800–9200 Å, with some gaps between the redder spectral orders. The star Gl 876 (M4 spectral type) was observed as an RV standard. The two-dimensional spectral images were processed with the MAKEE pipeline reduction package, written by Tom Barlow. These observations revealed that the eclipsing system was indeed a triple.

2.6 UVES spectroscopy

We obtained multi-epoch spectroscopy for NGTS J0002−29 between 2019 June and August with the red arm of UVES. The spectra were exposed on to a mosaic of two 2k × 4k CCDs (EEV + MIT/LL) with 15-μm pixels and a pixel scale of 0.182 arcsec per pixel. The resulting usable wavelength coverage extended from 6700 to 9850 Å with a gap of ∼100 Å at the centre. The observations were taken using a spectrograph slit width of 1.2 arcsec with a resolving power $\mathcal{R} \sim 40\,000$. We opted for 2 × 2 on-chip binning, giving median signal-to-noise (measured at the order centres for all orders and epochs) of 16.9 and 25.2 for the two respective CCDs. The data were reduced with the standard UVES pipeline recipes (Ballester et al. 2000) (version 5.10.4) via ESOREFLEX (Freudling et al. 2013), and we made use of both the individual Echelle orders and the merged spectra created. We downloaded raw data of the RV standard star GJ 109 (M3V spectral type; Henry et al. 2002) from the UVES archive [Program ID 074.B-0639(A) and $\mathcal{R} \sim 46\,000$] to be used as a template spectrum. The same reduction methods were implemented, producing spectra with median signal-to-noise of 284 and 217 for the two CCDs. GJ 109 appears in Nidever et al. (2002) with a velocity scatter below 0.1 km s^{-1}. It is also one of the validation stars used in the construction of the *Gaia* catalogue of RV standard stars (Soubiran et al. 2018), wherein 47 RVs collated from the SOPHIE spectrograph (Perruchot et al. 2008) show a standard deviation of 0.013 km s^{-1} over a 12-yr baseline. Extending the work of Nidever et al. (2002), Chubak et al. (2012) added to the catalogue of high-precision Keck-HIRES RV measurements for FGKM stars. For this work, we adopt the mean barycentric RV from Chubak et al. (2012) of 30.458 km s^{-1}. The listed standard deviation is 0.149 km s^{-1} over 11 measurements. This uncertainty, the standard error of the mean, or the formal uncertainties in the other catalogues are small compared with the known systematic uncertainties inherent to M-dwarf RVs, e.g. due to gravitational redshift and convective blueshift. This uncertainty is ∼0.3 km s^{-1} (Kraus et al. 2011; Chubak et al. 2012), which we adopt as the contribution from our template.

3 ANALYSIS

3.1 RVs

For the single HIRES observation, a traditional cross-correlation technique was used to reveal three spectral components in the system. As in Gillen et al. (2017, 2020a), RVs were derived using the FXCOR package within IRAF (Tody 1986) to correlate the spectrum of NGTS J0002−29 with that of the spectral standard observed on the same night, plus three other spectra of this same standard taken on different nights. This was done in order to improve the error on the measurement, since the night-to-night differences in the derived RVs are smaller than the order-to-order differences. Regions of telluric contamination were avoided within the wavelength range of 6330–7160 Å used in deriving the average velocities for the three components that are reported in Table 2. The velocities are the medians, while the uncertainties are the standard deviations among all standard spectra and orders.

We extracted the UVES RVs using the broadening function (BF) technique as introduced by Rucinski (1992, 1999, 2002).[4] The approach uses singular value decomposition (SVD) to determine the Doppler broadening kernel, *B*, from its assumed convolution with a template spectrum, *T*, when we observe target spectrum *S*:

$$S = B * T. \quad (1)$$

This method holds some advantages over the cross-correlation technique when analysing rotationally broadened spectra of binary or higher order systems. For example, while the cross-correlation function (CCF) inherits the common broadening components of both template and target star, such as instrumental, thermal, and micro-turbulence (Rucinski 1999), the BF isolates the rotational broadening contribution (assuming that the main difference between the target and template stars' spectra is attributable to rotation), and so offers superior resolution, as well as being less susceptible to the 'peak pulling' effect, which can be an issue when peaks overlap (Rucinski 2002; Hensberge & Pavlovski 2007; Kraus et al. 2011).

Rucinski provides IDL routines and a description of the method,[5] which we used as a basis for our own PYTHON implementation. We

[3] https://github.com/apchsh/SAFPhot

[4] Also introduced by Rix & White (1992) in the context of line-of-sight velocities of galaxies and applied to Doppler imaging of star-spots by Barnes (2004).

[5] http://www.astro.utoronto.ca/rucinski

Table 2. RVs for NGTS J0002−29.

Epoch			S/N[a]	RV (km s^{-1})			Instrument
UT date	BJD_{TDB}	Phase		Primary	Secondary	Tertiary	
2018-11-03	2458425.90890	0.116	19	− 33.13 ± 1.02	81.72 ± 2.27	10.42 ± 2.14	HIRES
2019-06-14	2458648.88849	0.193	21	− 54.85 ± 0.53	109.79 ± 0.80	5.28 ± 1.24	UVES
2019-07-06	2458670.86731	0.210	21	− 55.81 ± 0.55	114.10 ± 0.89	3.31 ± 1.22	UVES
2019-07-10	2458674.77115	0.765	21	67.94 ± 0.49	− 106.36 ± 0.73	4.97 ± 1.18	UVES
2019-07-10	2458674.89594	0.879	21	49.16 ± 0.42	− 72.60 ± 0.71	4.24 ± 0.86	UVES
2019-07-12	2458676.82505	0.636	20	53.36 ± 0.54	− 79.25 ± 0.91	5.90 ± 1.23	UVES
2019-08-02	2458697.76597	0.708	17	66.84 ± 0.51	− 102.52 ± 0.77	7.21 ± 1.27	UVES
2019-08-04	2458699.89145	0.643	21	55.06 ± 0.50	− 83.00 ± 0.84	6.19 ± 1.06	UVES
2019-08-10	2458705.87215	0.090	14	− 27.32 ± 0.55	64.96 ± 0.81	7.49 ± 1.24	UVES
2019-08-10	2458705.88096	0.098	13	− 30.49 ± 0.66	70.53 ± 1.04	7.96 ± 1.58	UVES

[a]HIRES S/N: at 7040 Å continuum. UVES S/N: median values based on orders used in the RV extraction (∼7800 Å).

refer the reader to the above (and to Rucinski 1992, 1999, 2002) for a detailed description, but we give a brief summary of the process here. The UVES observation times were converted to BJD (Barycentric Julian Date) format in the TDB (Barycentric Dynamical Time) time system, and barycentric corrections were computed. Each spectrum was continuum normalized using a cubic spline, with outliers ($+5\sigma$ and -8σ) removed using a rolling median filter. The spectra were re-sampled to a common wavelength vector in equal increments of log lambda with slight oversampling. Regions significantly affected by telluric lines were removed, before the BFs, with 301 bins, were computed with the SVD module in PYASTRONOMY (Czesla et al. 2019), and were smoothed with a Gaussian.

In the wavelength regime of our observations (6700–9850 Å), there is significant atmospheric absorption due to water and oxygen. Consequently, many Echelle orders were unsuitable for deriving RVs. Based on Cerro Paranal's yearly precipitable water vapour (Moehler et al. 2014) and ESO's Sky Model (Noll et al. 2012; Jones et al. 2013), and assuming airmass = 1.0 (closest available to our observations), we identified the wavelength regions in our UVES observations where atmospheric transmission was expected to be better than 95 per cent. With an additional criterion of a 50-Å minimum length, the resulting regions were contained in 12 Echelle orders, spanning approximately 6700–8880 Å.

The UVES pipeline merges Echelle orders into a single 1D spectrum: one for the lower CCD and one for the upper CCD. We trialled approaches using either individual orders or the merged spectrum, with very similar results, but we report values based on the merged spectrum, where the BFs were slightly better defined, yielding more precise RVs. This method took the merged spectrum from the lower CCD for each epoch and removed the telluric regions, leaving a single spectrum per epoch from which BFs were calculated. The usable spectral window was slightly smaller in this case (6750–8110 Å) due to the fact that the upper CCD was not incorporated. The segments of the merged spectrum used were as follows: 6740–6866, 7055–7150, 7386–7560, 7713–7894, and 8031–8110 Å. While this approach relies on sensible merging of orders in the UVES pipeline, it benefits from the target spectrum being significantly longer than the BF, which is advantageous because the quality of the determination of the BF increases in relation to how many times the spectrum is longer than the BF (Rucinski 2002).

A certain level of noise is invariably present along the baseline of BFs and CCFs. This underlying structure is worthwhile accounting for, because it can subtly affect the peak shapes and apparent centres from which the RVs are measured. To that end, and to assist in making robust uncertainty estimates, we chose to model the noise in the BFs with a Gaussian process (GP) at the same time as fitting for the peaks, an approach applied to CCFs in Gillen et al. (2014). Three clear peaks, suggestive of a triple system, are present in all spectra. Therefore, each BF was modelled as the sum of three Gaussians with a small constant offset, plus a GP with squared exponential kernel (see Fig. 2). All BFs were modelled simultaneously with 13 parameters fitted to each: height, width, and location of each Gaussian, vertical offset, two GP hyperparameters, and a small white noise term. The Gaussian profile widths were deemed to be constant between all BFs and so were jointly fitted. The posterior parameter space was explored using the affine invariant Markov chain Monte Carlo (MCMC) method implemented in EMCEE (Foreman-Mackey et al. 2013), with 500 'walkers'. The parameter values were initialized around estimates from a simple three-Gaussian fit and some trial runs. The chains were run for 200 000 steps; the first 100 000 steps were discarded as 'burn-in', and each chain was thinned based on the average autocorrelation time. The GP component was handled with the GEORGE package (Ambikasaran et al. 2015). In Table 2, we report the median samples from the relevant marginalized distributions as the UVES RVs. Our adopted uncertainty for each RV is the mean of the values corresponding to the 16th and 84th percentiles (which are always consistent at the 1–2 per cent level), plus the estimated uncertainty for the template star of 0.3 km s^{-1}, added in quadrature. In the global model, the UVES and HIRES RVs were modelled using Keplerian orbits. A jitter term was fitted to the UVES RVs, along with an offset term for the single HIRES observation in order to account for the difference between instrument zero-points.

The BF methodology was additionally applied to the derivation of spectroscopic light ratios from the UVES spectra, which were subsequently used as constraints in the global modelling. These light ratios were determined by measuring the areas under the Gaussian peaks fitted to the BFs. This was done for three wavelength segments across the UVES spectra: 6740–7150, 7386–8110, and 8690–8882 Å. For each segment, we computed BFs for all epochs and fitted them with the GP + three-Gaussian model described previously. We then measured the area under each Gaussian peak and computed the final light ratios by taking an inverse-variance weighted mean for each wavelength region, propagating the uncertainties through from the MCMC fit. The values determined for the binary and tertiary light ratios are shown in Table 3, where the quoted uncertainties are the standard errors of the weighted means, $\left(\sqrt{\sum_{i=1}^{n} w_i}\right)^{-1}$.

3.2 Global modelling

The global modelling was performed with GP-EBOP, an EB and transiting planet model that is optimized for modelling young and/or

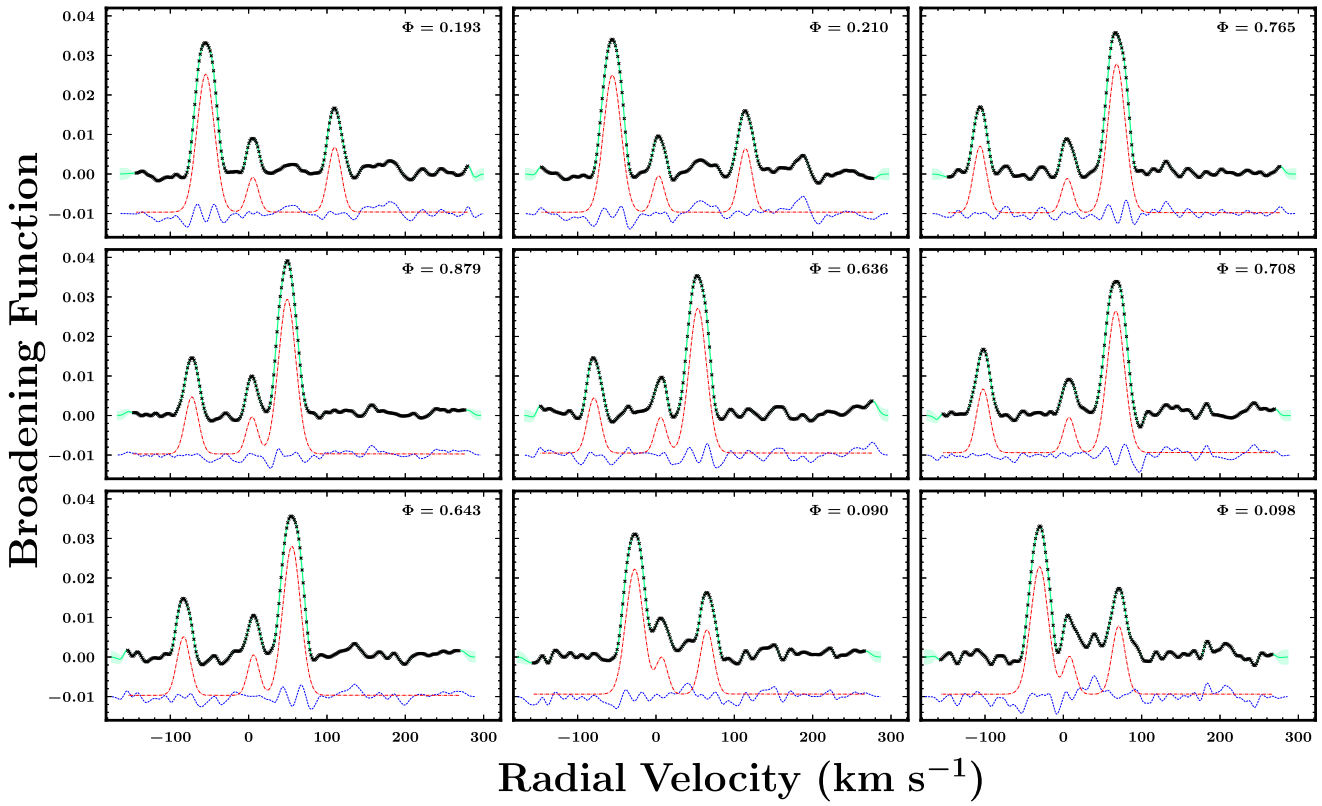

Figure 2. BFs (black crosses) from our UVES spectra at each epoch in observation order, with the orbital phases labelled. Each plot shows the best-fitting model (green) together with the associated 68.3 per cent confidence interval (light green shaded region). The Gaussian (red dot–dashed line) and GP (blue dashed line) terms are also displayed, with a vertical offset added for clarity. The tallest peak in each plot corresponds to the primary component, while the second and third tallest peaks correspond to the secondary and tertiary components, respectively.

Table 3. Binary and tertiary light ratios from UVES spectra.

Wavelength region Å	Binary light ratio $l_{\rm sec}/l_{\rm pri}$	Tertiary light ratio $l_{\rm ter}/(l_{\rm pri}+l_{\rm sec}+l_{\rm ter})$
6740–7150	0.30 ± 0.01	0.10 ± 0.01
7386–8110	0.37 ± 0.01	0.15 ± 0.01
8690–8882	0.38 ± 0.02	0.15 ± 0.01

active systems. We give a brief description here, but refer readers to Gillen et al. (2017, 2020a) for more details.

GP-EBOP permits simultaneous modelling of light curves, RVs, and SEDs, using a GP framework to model the out-of-eclipse (OOE) variations and stellar activity. The GP model means that uncertainties in the variability modelling can be propagated through to the posterior distributions for the EB parameters. GP-EBOP uses an EB model based on that described in Irwin et al. (2011, 2018), which is a descendent of the EBOP family of models, but which uses the analytical method of Mandel & Agol (2002) to perform the eclipse calculations. Limb darkening is parametrized using the triangular sampling method of Kipping (2013), with theoretical constraints applied based on the predictions of the Limb Darkening Toolkit (Parviainen & Aigrain 2015). The posterior parameter space is explored using EMCEE.

There are two main updates to GP-EBOP since Gillen et al. (2020a):

(i) The GP model can now optionally use the CELERITE2 library (Foreman-Mackey 2018), as well as CELERITE (Foreman-Mackey et al. 2017) and GEORGE.

(ii) GP-EBOP is able to simultaneously model the component SEDs of triple systems.

For the analysis presented here, we simultaneously modelled the observed light curves, RVs, and SED of NGTS J0002−29.

3.3 Light curves

The NGTS light curve (see Fig. 1) was sigma clipped outside of the eclipses on a nightly basis with a 5σ (sigma = 1.4826 × Median Absolute Deviation) threshold. The time array was converted to $\rm BJD_{TDB}$ with ASTROPY (Astropy Collaboration 2013, 2018) and then the light curve was median normalized and binned in time to 10 min. An additional 5σ nightly clipping was applied to the binned light curve, as well as the removal of two nights badly affected by adverse observing conditions. As is evident from Fig. 1, the system displays a gentle modulation in flux on the orbital period, which peaks around primary eclipse. The peak-to-trough variation is 1.8 per cent and 1.2 per cent in the NGTS and *TESS* light curves, respectively. The most likely cause of this modulation is star-spots, which explains the difference in amplitudes between NGTS and *TESS* (the *TESS* passband being redder). The low-amplitude signal suggests that any longitudinal inhomogeneities on the stellar surfaces are modest. We also find a little variability in phase with the lunar cycle, a consequence of imperfect background subtraction known to affect fainter (NGTS $\gtrsim$ 15 mag) targets. For the GP component of the model, we chose the rotation kernel implemented in CELERITE2, which is a good descriptive model for a wide range of stochastic variability in stellar time series, including rotational modulation. The

kernel is a mixture of two stochastically driven, damped harmonic oscillator (SHO) terms. The power spectral density of the SHO term is given by

$$S(\omega) = \sqrt{\frac{2}{\pi}} \frac{S_0 \, {\omega_0}^2}{(\omega^2 - {\omega_0}^2)^2 + {\omega_0}^2 \, \omega^2 / Q^2}, \quad (2)$$

where ω is the angular frequency, S_0 is the amplitude of the oscillation, ω_0 is the un-damped frequency, and Q is the quality factor. We checked that the resulting interpolations across each eclipse were satisfactory, with the eclipse depths maintained before and after detrending for the GP component. We initialized the MCMC sampler using the well-determined ephemeris, with wide uniform priors placed on all GP hyperparameters.

The GP kernel adopted for the *TESS*, SPECULOOS, and SAAO light curves was a single SHO term with $Q = 1/\sqrt{2}$. The *TESS* light curve was sigma clipped outside of the eclipses using a median filter and a 10σ threshold, which removed two outlier points. We considered the uncertainties from ELEANOR to be too large given the scatter, and so calculated our own for each data point, i, as

$$\sigma_{i,\mathrm{new}} = 1.4826 \times \mathrm{MAD}_{\mathrm{OOE}} \times \frac{\sigma_{i,\mathrm{old}}}{\mathrm{median}(\sigma_{\mathrm{old}})}. \quad (3)$$

The high-precision SPECULOOS observations contain single primary and secondary eclipses. The data displayed ramps in flux at the start of each night, which are characteristic of ground-based observations looking through high airmass. Accordingly, the first six data points taken in each night were removed before modelling.

The SAAO light curve was sigma clipped using a median filter and a 5σ threshold. Diagnostic plots from the observations revealed movement across the CCD, as well as variations in the background flux taking place during eclipse. We attribute the slight asymmetry in the eclipse shape to these effects. We also note that the inclusion of the SAAO light curve led to greater uncertainty in the derived radius of the secondary. This could be explained by the fact that the noise and asymmetry found in the SAAO secondary eclipse are not present in any of the other light curves, and so the global model does not significantly change to account for these features. The consequent poorer fit to the SAAO light curve has the effect, however, of increasing the uncertainties. Our intention with the *V*-band SAAO observations was to have a constraint in a bluer spectral region, which might break the degeneracy between radius ratio, inclination, and surface brightness, thought to be the cause of the poorly constrained radius ratio we obtained when modelling the light curves and RVs without the SED. However, bad weather thwarted attempts to obtain a primary eclipse with SAAO, leaving this constraint unrealized. We include the secondary eclipse in our global model none the less.

3.3.1 Gravity darkening

We adopted gravity darkening coefficients from the tables of Claret & Bloemen (2011) for $\log g = 5.0$, solar metallicity, *I*-band filter, and PHOENIX atmosphere models, interpolating to the temperatures of each binary component. These tables give the required input to the central EB model (Irwin et al. 2018).

3.4 SED

Table 4 reports our collected broad-band photometric measurements that we used to model the SED of NGTS J0002−29. This photometry covers the rise, peak, and fall of the combined stellar photospheric emission spectra, thus providing useful constraints on the effective temperatures.

We modelled the observed SED of NGTS J0002−29 as the sum of three stellar photospheres (primary, secondary, and tertiary components). Model grids of BT-Settl model atmospheres (Allard, Homeier & Freytag 2012) were convolved with the spectral response functions of each band to create a grid of model fluxes in steps of 100 K in effective temperature and 0.5 in surface gravity over ranges of $1200 \leq T_{\mathrm{eff}} \leq 7000$ and $3.0 \leq \log g \leq 5.5$, respectively. Each SED was modelled by interpolating the model grids with a cubic spline in T_{eff}–$\log g$ space, keeping metallicity fixed at $Z = 0.0$. The observed magnitudes were converted to spectral flux densities using standard relations, with the zero-point values and effective wavelengths obtained from the references in Table 4. The parameters of the fit were: the temperatures, radii and surface gravities of both stars, the distance and reddening to the system, and a jitter term per photometric data set. The reddening model follows the extinction law of Fitzpatrick (1999) with the improvements made by Indebetouw et al. (2005).

Simultaneously modelling the SED, along with the light curves and RVs, enables measurements of the spectroscopic light ratios (as described in Section 3.1) to constrain the eclipse modelling in the observed light curve bands. It also means that we solve for the stellar masses, radii, and temperatures in a self-consistent manner. We implemented the spectroscopic light ratios by applying prior constraints on the model binary ($l_{\mathrm{sec}}/l_{\mathrm{pri}}$) and tertiary [$l_{\mathrm{ter}}/(l_{\mathrm{pri}} + l_{\mathrm{sec}} + l_{\mathrm{ter}})$] light ratios within the UVES band. Those constraints were propagated into the eclipse modelling by using the corresponding atmospheric model ratios of emergent stellar fluxes and luminosities in the NGTS, *TESS*, SPECULOOS, and SAAO bands as the central surface brightness ratios and third light parameters given to the central EB model. In the case of *TESS*, we fitted for an extra third light component (added to the model tertiary light ratio), due to the eclipse dilution previously described. We allowed the light ratio uncertainties to inflate by fitting jitter terms to each. These were added to account for any additional uncertainties in the measurement procedure, e.g. from the use of BFs and Gaussian fits; the use of a single spectroscopic template that cannot be a perfect match to all three stellar components; and the use of stellar atmosphere models. A modified Jeffreys prior was placed on each jitter term, with the 'knee' value set to twice the calculated uncertainty of the corresponding light ratio, and the upper bound set to 0.5. The propagation of these spectroscopic constraints helped to break the degeneracy between radius ratio, inclination, and surface brightness.

The use of light ratios derived from spectral lines as proxies for broad-band flux ratios is reasonable when the stars in question have similar spectral characteristics, but it can pose potential problems in other cases. That is, for stars with significantly different spectral types, and hence differing line strengths, spectroscopic light ratios may be inadequate representations of passband-integrated light ratios. For the present case of three mid–late M dwarfs, where we use wide spectral windows for the calculation of the BFs, which should help in averaging out any differences in particular spectral lines, we expect the approach to be valid.

The use of stellar atmosphere models to predict flux ratios between stars in different photometric bands means that a model dependence is introduced. While this is not an ideal approach for the derivation of EB parameters, we expect the model dependence to be small, because while atmosphere models do not reproduce all spectral lines and features, they should be able to provide reasonable constraints on the flux ratios between two or three model atmospheres in wide photometric bands, such as those of our observations and broad-band photometry. We note that a test case for this method appeared in Gillen et al. (2020a), where a comparison was made – for a

Table 4. Broad-band photometry constituting the observed SED of NGTS J0002−29.

Band	System	Magnitude	Spectral flux density (erg s^{-1} cm^{-2} Å^{-1})	Refs.
Pan-STARRS1 *g*	AB	18.0980 ± 0.0077	(2.669 ± 0.019) × 10^{-16}	(1, 7, 8)
Pan-STARRS1 *r*	AB	16.9314 ± 0.0025	(4.779 ± 0.011) × 10^{-16}	(1, 7, 8)
Pan-STARRS1 *i*	AB	15.5682 ± 0.0029	(1.136 ± 0.003) × 10^{-15}	(1, 7, 8)
Pan-STARRS1 *z*	AB	14.9537 ± 0.0018	(1.510 ± 0.003) × 10^{-15}	(1, 7, 8)
Pan-STARRS1 *y*	AB	14.6535 ± 0.0027	(1.616 ± 0.004) × 10^{-15}	(1, 7, 8)
APASS *g*	AB	18.331 ± 0.254	(2.322 ± 0.543) × 10^{-16}	(2, 7)
APASS *r*	AB	16.903 ± 0.211	(4.977 ± 0.967) × 10^{-16}	(2, 7)
APASS *i*	AB	15.509 ± 0.222	(1.220 ± 0.250) × 10^{-15}	(2, 7)
SkyMapper *g*	AB	17.9057 ± 0.0440	(2.964 ± 0.120) × 10^{-16}	(3, 7)
SkyMapper *r*	AB	16.9722 ± 0.0124	(4.756 ± 0.054) × 10^{-16}	(3, 7)
SkyMapper *i*	AB	15.4421 ± 0.0048	(1.207 ± 0.005) × 10^{-15}	(3, 7)
SkyMapper *z*	AB	14.8559 ± 0.0084	(1.496 ± 0.012) × 10^{-15}	(3, 7)
Gaia G	Vega	16.40242 ± 0.00453	(7.8466 ± 0.0328) × 10^{-16}	(4, 7, 9)
Gaia G_{BP}	Vega	17.78037 ± 0.01058	(3.2435 ± 0.0316) × 10^{-16}	(4, 7, 9)
Gaia G_{RP}	Vega	15.08023 ± 0.00467	(1.2252 ± 0.0053) × 10^{-15}	(4, 7, 9)
2MASS *J*	Vega	13.434 ± 0.029	(1.324 ± 0.035) × 10^{-15}	(5, 7, 10)
2MASS *H*	Vega	12.829 ± 0.023	(8.371 ± 0.177) × 10^{-16}	(5, 7, 10)
2MASS K_s	Vega	12.556 ± 0.024	(4.067 ± 0.090) × 10^{-16}	(5, 7, 10)
WISE W1	Vega	12.444 ± 0.023	(8.693 ± 0.184) × 10^{-17}	(6, 7)
WISE W2	Vega	12.271 ± 0.023	(3.002 ± 0.064) × 10^{-17}	(6, 7)

Note. References. *Photometry:* 1. Chambers et al. (2016); 2. Henden (2019); 3. Onken et al. (2019); 4. Gaia Collaboration (2020); 5. Skrutskie et al. (2006); 6. Wright et al. (2010). *Bandpasses:* 7. Filter Profile Service (FPS: http://svo2.cab.inta-csic.es/theory/fps); 8. Tonry et al. (2012); 9. Riello et al. (2021); 10. Cohen, Wheaton & Megeath (2003).

system without significant degeneracies in radius ratio, inclination, and surface brightness – between modelling the light curves and RVs only, and also modelling the SED; consistent masses and radii were found. We also note that, of the fundamental parameters, it is only the radius that is in any meaningful way subject to additional model dependence compared with standard EB parameter derivation; for example, the masses are almost entirely constrained by the RVs, and individual effective temperatures are always reliant on theoretical and/or empirical relations, or else SED modelling as performed here.

4 RESULTS

We simultaneously modelled the NGTS, *TESS*, SPECULOOS, and SAAO light curves, UVES and HIRES RVs, and system SED with GP-EBOP. We used 400 'walkers' to explore parameter space in the MCMC. The chains were run for 400 000 steps; the first 100 000 steps were discarded as burn-in, and each chain was thinned based on the average autocorrelation time.[6]

Figs 3–5 display the model fits to the data. Fig. 3 shows each light curve with the global GP-EBOP model. The figure also shows, for NGTS and *TESS*, the light curves detrended with respect to the GP and phase folded on the binary period, accompanied by close-ups of the eclipses. The RV orbit solution is shown in Fig. 4, phase folded on the orbital period of the binary. The sinusoidal curves indicate a negligible eccentricity, as expected given the period. The measured RVs of the tertiary component are also plotted. The derived systemic velocity is 5.39 ± 0.18 km s^{-1} (dashed grey line), and we measure the weighted-mean RV of the tertiary component as 5.63 ± 0.38 km s^{-1}. These values are encouragingly similar to the estimate for the Blanco 1 cluster-centre RV (5.78 ± 0.10 km s^{-1}; G18), and bode well for our assumption that the tertiary is physically associated with the binary. The system SED is plotted in Fig. 5, showing the BT-Settl model fit to the observed broad-band magnitudes and the derived SEDs of each component. The system geometry at primary and secondary eclipses is depicted in Fig. 6, where we see a grazing eclipse – something in-keeping with the poor constraints on the radius ratio found prior to our SED modelling. The main parameters of the fit are given in the top section of Table 5, with derived parameters in the middle and bottom sections.

We find the masses, radii, and effective temperatures of the binary components in NGTS J0002−29 to be: $M_{pri} = 0.3978 \pm 0.0033$ M$_\odot$, $M_{sec} = 0.2245 \pm 0.0018$ M$_\odot$, $R_{pri} = 0.4037 \pm 0.0048$ R$_\odot$, $R_{sec} = 0.2759 \pm 0.0055$ R$_\odot$, $T_{pri} = 3372^{+44}_{-37}$ K, and $T_{sec} = 3231^{+38}_{-31}$ K, respectively. For the tertiary, we find $R_{ter} = 0.25 \pm 0.03$ R$_\odot$ and $T_{ter} = 3183^{+93}_{-104}$ K. We note that our effective temperatures have a strong dependence on the particular stellar atmosphere models used (although our masses and radii do not). We present our main results using BT-Settl model atmospheres, but compare with the PHOENIX model atmospheres of Husser et al. (2013) in Section 5.7.

5 DISCUSSION

5.1 Mass–radius relation for low-mass EBs

Fig. 7 shows the mass–radius relation for detached, double-lined, stellar-mass EBs below 1.5 M$_\odot$. The coloured lines represent the Baraffe et al. (2015) isochrones (hereafter BHAC15) from 1 Myr to 1 Gyr, and the data points show measurements for EBs in the field (grey) and in sub-Gyr open clusters (coloured; see figure caption for colour scheme). NGTS J0002−29 is shown with yellow stars. The sub-Gyr cluster EBs represent some of the best tests of stellar evolution theory at low masses and young ages; NGTS J0002−29 brings the total in this ensemble to 20. The inset to Fig. 7 shows a

[6]We also ran tests with the ensemble slice sampling MCMC method implemented in `zeus` (Karamanis, Beutler & Peacock 2021), with almost identical results.

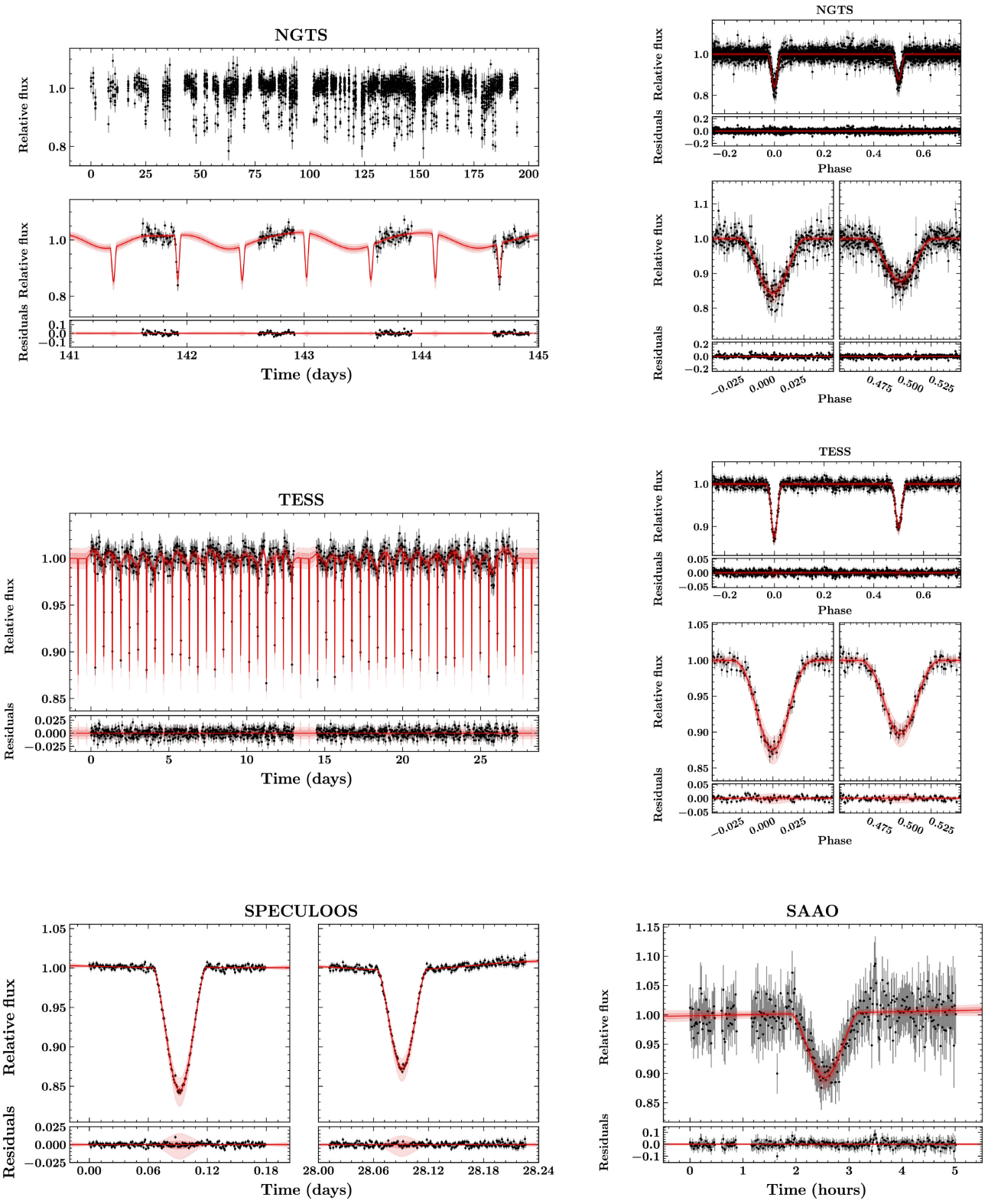

Figure 3. Top left: NGTS relative flux light curve of NGTS J0002−29 (binned to 10 min), with a 4-d close-up in the lower panel showing the GP-EBOP model in red and residuals below. The red line and pink shaded regions show the mean and 1σ and 2σ confidence intervals of the predictive posterior distribution. Centre left: As above, but for the *TESS* observations. In this case, the GP model is overlaid on the whole light curve. Bottom left and right show equivalent plots for SPECULOOS and SAAO light curves, respectively. Top and centre right: Phase-folded light curves from NGTS and *TESS*, respectively, which have been detrended with respect to the GP model. The red line indicates the median EB model derived from the posterior distribution; i.e. individual draws are calculated across phase space and the median of their paths plotted. Phase zero marks the centre of the primary eclipse. Immediately below are the residuals of the fit. The lower panels display zooms on primary and secondary eclipses (left and right, respectively) with the median model and 1σ and 2σ uncertainties shown (red line and pink shaded regions, respectively). Residuals are shown immediately below.

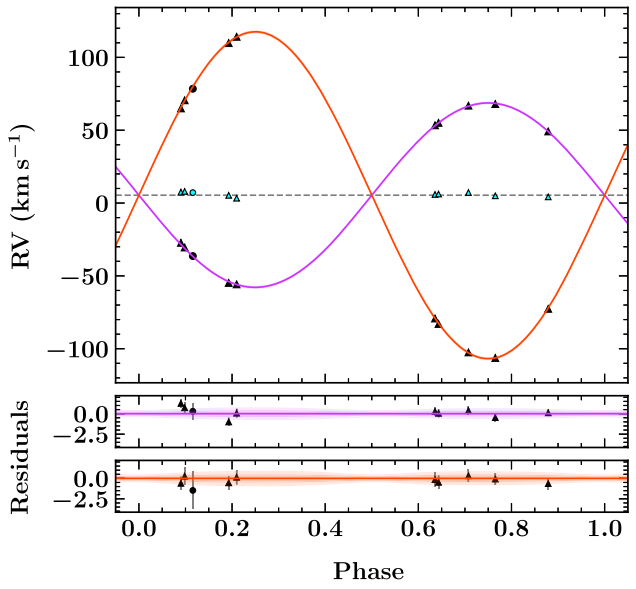

Figure 4. Top: phase-folded RV orbit of NGTS J0002−29 with UVES (triangles) and HIRES (circles) RV measurements for the primary and secondary stars (purple and orange, respectively). The lines and shaded regions indicate the median and 2σ uncertainty on the posterior distribution of the RV orbits. The tertiary component RVs are plotted with cyan markers and the grey horizontal dotted line indicates the systemic velocity. Bottom: residuals of the fit.

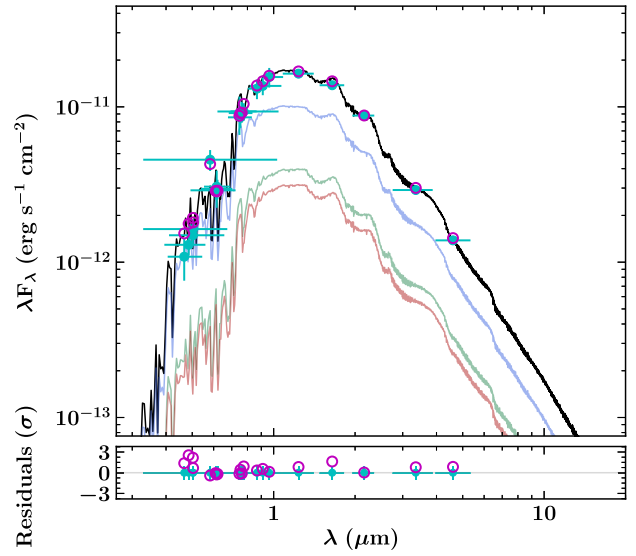

Figure 5. SED of NGTS J0002−29. Cyan points represent the observed broad-band magnitudes reported in Table 4, which together comprise the observed SED. The horizontal cyan error bars indicate the spectral range of each band. SEDs constructed from BT-Settl model atmospheres for the primary, secondary, and tertiary stars are shown in blue, green, and red, respectively. Their combined SED is shown in black, with its prediction in each observed band indicated by magenta circles. Residuals are shown below.

close-up of the region around NGTS J0002−29, and it is apparent that the primary has a larger radius than the three field stars most similar in mass. The inset also displays the only well-characterized low-mass EB from the Pleiades (HCG 76; David et al. 2016) (magenta markers), where the LDB age estimates of 125 ± 8 Myr (Stauffer,

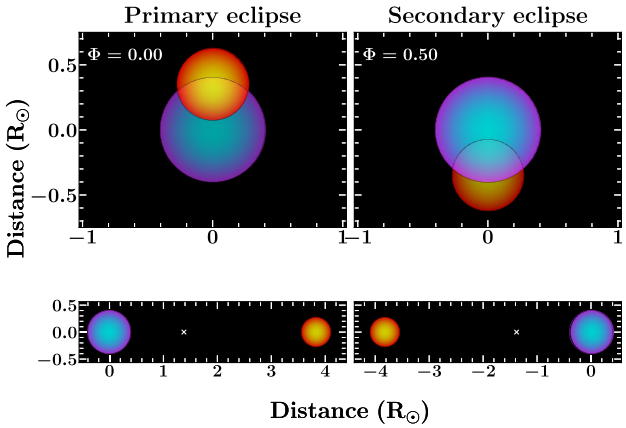

Figure 6. System geometry of NGTS J0002−29 to scale at primary and secondary eclipses (left- and right-hand panels, respectively). The primary star is shown in purple/blue and the secondary in orange/yellow, with the orbital phases labelled. The upper panels display our view with the primary star at the origin, while the lower panels give a side-on perspective in the orbital plane, perpendicular to a straight line joining the stars, to show the separation. The centre of mass is marked by a white cross.

Schultz & Kirkpatrick 1998) and 112 ± 5 Myr (Dahm 2015) are similar to Blanco 1. Its components (like the NGTS J0002−29 primary) prefer younger-than-canonical ages when compared with the BHAC15 isochrones.

5.2 Context

In addition to its main use as a test of stellar evolution theory, the properties of NGTS J0002−29 place it within three interesting sub-groups of the known double-lined EB population: (1) those with low mass ratios, (2) those with known tertiary companions, and (3) those with components that span the fully convective boundary (see Fig. 8). Although membership of any one of these sub-groups is not an exceptionally rare trait, membership of all three is (to the best of our knowledge) unique for a well-characterized cluster EB. Binary mass ratios are relevant to the study of stellar evolution, with low-mass-ratio EBs ensuring that model predictions are tested over a wide range of masses for a single metallicity and age. The presence of tertiary companions is also relevant to stellar evolution and has been linked to particularly large model–observation discrepancies (Stassun et al. 2014), while differences in energy transport for components spanning the fully convective boundary should provide stringent tests of evolutionary models. We therefore discuss these topics, before comparing the measured and derived properties of NGTS J0002−29 with stellar evolution models.

5.2.1 Mass ratios

The distribution of binary mass ratios ($q = M_{\rm sec}/M_{\rm pri}$) should contain information about the components' formation and early evolution. If a protobinary forms within a collapsing molecular cloud core, the final masses will depend on how the stars accrete and interact with the surrounding material. One well-subscribed idea is that, in such a scenario, mass ratios will tend to be biased towards unity and that low-mass ratios will be rare for short-period systems, compared with longer period binaries (Bate & Bonnell 1997; Bate 2000; Young & Clarke 2015). One of the reasons for this is that the specific angular momentum of infalling material is higher, relative to

Table 5. Fitted and derived parameters for NGTS J0002−29.

Parameter	Symbol	Value	Unit
	Fitted physical parameters		
Orbital period	P	$1.098\,005\,24 \pm 0.000\,000\,38$	days
Time of primary eclipse centre	$T_{\rm prim}$	$2457\,998.657\,72 \pm 0.000\,15$	BJD
Sum of radii	$(R_{\rm pri} + R_{\rm sec})/a$	0.1777 ± 0.0017	–
Radius ratio	$R_{\rm sec}/R_{\rm pri}$	0.684 ± 0.015	–
Cosine of orbital inclination	$\cos i$	$0.0913^{+0.0028}_{-0.0033}$	–
Eccentricity and argument of-	$\sqrt{e}\cos\omega$	$0.0071^{+0.0062}_{-0.0050}$	–
-periastron combination terms	$\sqrt{e}\sin\omega$	-0.005 ± 0.031	–
Systemic velocity	$V_{\rm sys}$	5.39 ± 0.18	km s^{-1}
Primary RV semi-amplitude	$K_{\rm pri}$	63.31 ± 0.26	km s^{-1}
Secondary RV semi-amplitude	$K_{\rm sec}$	112.17 ± 0.38	km s^{-1}
Distance	d	$227.8^{+5.8}_{-5.5}$	pc
Reddening	$A_{\rm V}$	$0.045^{+0.086}_{-0.035}$	–
Primary effective temperature	$T_{\rm pri}$	3372^{+44}_{-37}	K
Secondary effective temperature	$T_{\rm sec}$	3231^{+38}_{-31}	K
Tertiary effective temperature	$T_{\rm ter}$	3183^{+93}_{-104}	K
	Derived fundamental parameters		
Primary mass	$M_{\rm pri}$	0.3978 ± 0.0033	M$_\odot$
Secondary mass	$M_{\rm sec}$	0.2245 ± 0.0018	M$_\odot$
Primary radius	$R_{\rm pri}$	0.4037 ± 0.0048	R$_\odot$
Secondary radius	$R_{\rm sec}$	0.2759 ± 0.0055	R$_\odot$
Tertiary radius	$R_{\rm ter}$	0.25 ± 0.03	R$_\odot$
Primary luminosity	$L_{\rm pri}$	0.019 ± 0.001	L$_\odot$
Secondary luminosity	$L_{\rm sec}$	0.0075 ± 0.0005	L$_\odot$
Primary surface gravity	$\log g_{\rm pri}$	4.826 ± 0.010	(cm s^{-2})
Secondary surface gravity	$\log g_{\rm sec}$	4.908 ± 0.017	(cm s^{-2})
Mass sum	$M_{\rm pri} + M_{\rm sec}$	0.6223 ± 0.0048	M$_\odot$
Radius sum	$R_{\rm pri} + R_{\rm sec}$	$0.6797^{+0.0064}_{-0.0069}$	R$_\odot$
	Derived radiative, orbital, and rotational parameters		
Central surface brightness ratio in NGTS	$J_{\rm NGTS}$	0.744 ± 0.015	–
Central surface brightness ratio in *TESS*	$J_{\rm TESS}$	0.792 ± 0.012	–
Central surface brightness ratio in SPECULOOS $I + z'$	$J_{\rm SPECULOOS}$	0.813 ± 0.011	–
Central surface brightness ratio in SAAO V	$J_{\rm SAAO}$	0.629 ± 0.020	–
Third light in NGTS	$L3_{\rm NGTS}$	0.154 ± 0.003	–
Third light in *TESS*	$L3_{\rm TESS}$	0.249 ± 0.003	–
Third light in SPECULOOS $I + z'$	$L3_{\rm SPECULOOS}$	0.167 ± 0.003	–
Third light in SAAO V	$L3_{\rm SAAO}$	0.131 ± 0.002	–
Semimajor axis	a	3.8239 ± 0.0099	R$_\odot$
Orbital inclination	i	$84.76^{+0.19}_{-0.16}$	$^\circ$
Eccentricity	e	$0.00052^{+0.00130}_{-0.00034}$	–
Longitude of periastron	ω	272^{+32}_{-215}	$^\circ$
Primary synchronized velocity	$V_{\rm pri\ sync}$	18.60 ± 0.22	km s^{-1}
Secondary synchronized velocity	$V_{\rm sec\ sync}$	12.71 ± 0.25	km s^{-1}

the binary, when the separation between the two stars is smaller, and accretion is preferentially directed towards the lower mass secondary when that material has high angular momentum. At low angular momentum, gas falls towards the centre of mass of the system and so is accreted mainly by the primary, but with increasing angular momentum, circumstellar discs may form around primary and secondary, leading to more accretion by the secondary. With sufficient angular momentum, a circumbinary disc forms – with an inner edge closer to the secondary – and accretion will tend to drive the mass ratio towards 1. The relative accretion rate of secondary to primary in the presence of a circumbinary disc is a strong function of the initial mass ratio, with low mass ratios heavily favouring the secondary (Bate & Bonnell 1997). Alternatives to this mechanism have been proposed that instead favour accretion on to the primary (Ochi, Sugimoto & Hanawa 2005; Hanawa, Ochi & Ando 2009; de Val-Borro et al. 2011), but the assumed gas temperatures in those simulations could be too high to be representative of stellar binaries; at lower temperatures, accretion would still favour the secondary (Young & Clarke 2015).

The other main reason for the expectation of few extreme mass ratios in close binary systems is one of dynamics. In the early stages of a binary system's life, interactions with other stars formed from the same or nearby cores are more likely than at later times, when the star-forming regions are dispersed. Such interactions, as demonstrated by simulations, are expected to lead to the ejection of the least massive component. This would naturally lead to an equalization of masses and to massive stars being more likely to have close companions than lower mass stars (Bate, Bonnell & Bromm 2002). Finally, higher

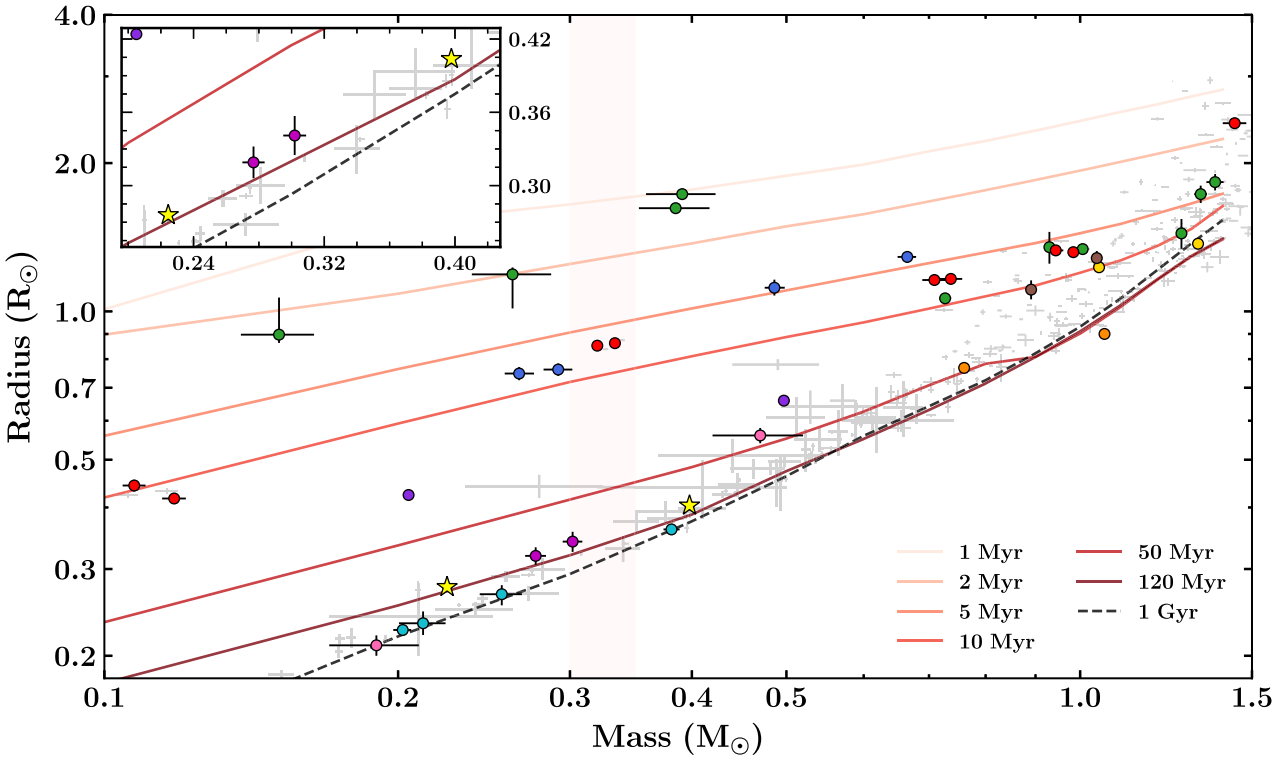

Figure 7. Mass–radius relation for detached, double-lined, stellar-mass EBs below 1.5 $M_\odot$. The coloured lines represent the solar metallicity isochrones of BHAC15 from 1 Myr to 1 Gyr (light-to-dark, top-to-bottom). Well-characterized EBs in sub-Gyr open clusters are coloured, while field EBs are shown in grey. NGTS J0002−29 is plotted with yellow stars, with other cluster EBs shown in green (Orion), red (Upper Scorpius; including the eclipsing triple HD 144548), pink (NGC 1647), gold (Per OB2), magenta (Pleiades), orange (Hyades), cyan (Praesepe), brown (Upper Centaurus Lupus), blue (NGC 2264), and violet (32 Orionis Moving Group). The fully convective boundary is represented by a pink vertical bar. The cluster EBs (uncertainties $\lesssim$10 per cent; component masses $<$1.5 $M_\odot$; ages $<$1 Gyr) are as compiled by Gillen et al. (2017), with subsequent additions from Gómez Maqueo Chew et al. (2019), David et al. (2019), Murphy et al. (2020), and Gillen et al. (2020a). The field sample comprises the DEBCat catalogue (mass and radius uncertainties $<$2 per cent; Southworth 2015); the close ($P < 10$ d) systems with M-dwarf primaries collected by Nefs et al. (2013) (non-detached systems removed); and additional EBs from Irwin et al. (2009, 2018), Stassun, Feiden & Torres (2014), Zhou et al. (2015), Dittmann et al. (2017), Casewell et al. (2018), and Miller et al. (2021). Inset: zoom on the region around NGTS J0002−29.

mass-ratio binaries have higher binding energies and so are more resistant to disruption (El-Badry et al. 2019).

Observationally testing theories about binary mass ratios has been challenging historically. Duchêne & Kraus (2013) note, in their review on stellar multiplicity, how the difficulties associated with the detection of low-mass companions have led to widely discrepant conclusions (see e.g. Trimble 1990). Modern volume-limited surveys, with their large sample sizes, are promising means of achieving more reliability. In such studies (e.g. Raghavan et al. 2010; Moe & Di Stefano 2017; El-Badry et al. 2019), significant excess twin fractions, $\mathcal{F}_{\rm twin}$, (*twin* meaning $q > 0.95$), at shorter periods are indeed found, in line with theoretical expectations.

In the low-mass domain, Bergfors et al. (2010) found evidence for a peak at $q \gtrsim 0.7$–0.8 in the mass ratio distribution of mid-type M dwarfs (M 3.5–M 5.5), but not for early M dwarfs. Nefs et al. (2013) analysed the mass ratio distribution of known M-dwarf binaries, finding that over 80 per cent of stellar binaries have $q \geq 0.8$, although they noted how low-mass, low-luminosity companions may be unresolved in optical spectroscopy and so bias the distribution towards equal mass ratios. As El-Badry et al. (2019) explain, the bias against low-mass companions is a feature of all binary detection methods; for example, low-mass stars induce weaker RV shifts for a given separation, contribute less light to observed spectra, and create shallower eclipses, and are less likely to be detected as part of visual binaries. Additionally, the detection efficiency varies with primary mass and separation, which makes attempts to correct for incompleteness and bias all the more challenging. At even later spectral types (M 7–M 9.5), recent work, based on a large homogeneous sample from Ahmed & Warren (2019), has suggested that almost all unresolved binaries are likely to be twins (Laithwaite & Warren 2020). However, the NGTS discovery of an M dwarf EB with a mass ratio $q = 0.14$ and $M_{\rm sec} = 0.08\,M_\odot$ (Acton et al. 2020b) highlights that extreme mass ratios do exist.

In the top plot of Fig. 8, we show binary mass ratio as a function of orbital period for detached, double-lined, stellar-mass EBs. There is visible clustering of systems towards $q \approx 1.0$, with a median mass ratio of $q = 0.92$. The mass ratio of NGTS J0002−29 ($q = 0.564 \pm 0.003$) is smaller than ∼95 per cent of the systems shown, and, while not extreme, does place it in a fairly sparsely populated region of the diagram.

5.2.2 *Triple systems and the tertiary component*

Tokovinin et al. (2006) found that the vast majority (96 per cent) of solar-type spectroscopic binaries with periods shorter than 3 d have an additional companion, a result with recent corroboration from Laos, Stassun & Mathieu (2020). In both studies, the frequency of triple systems was found to be a strong function of

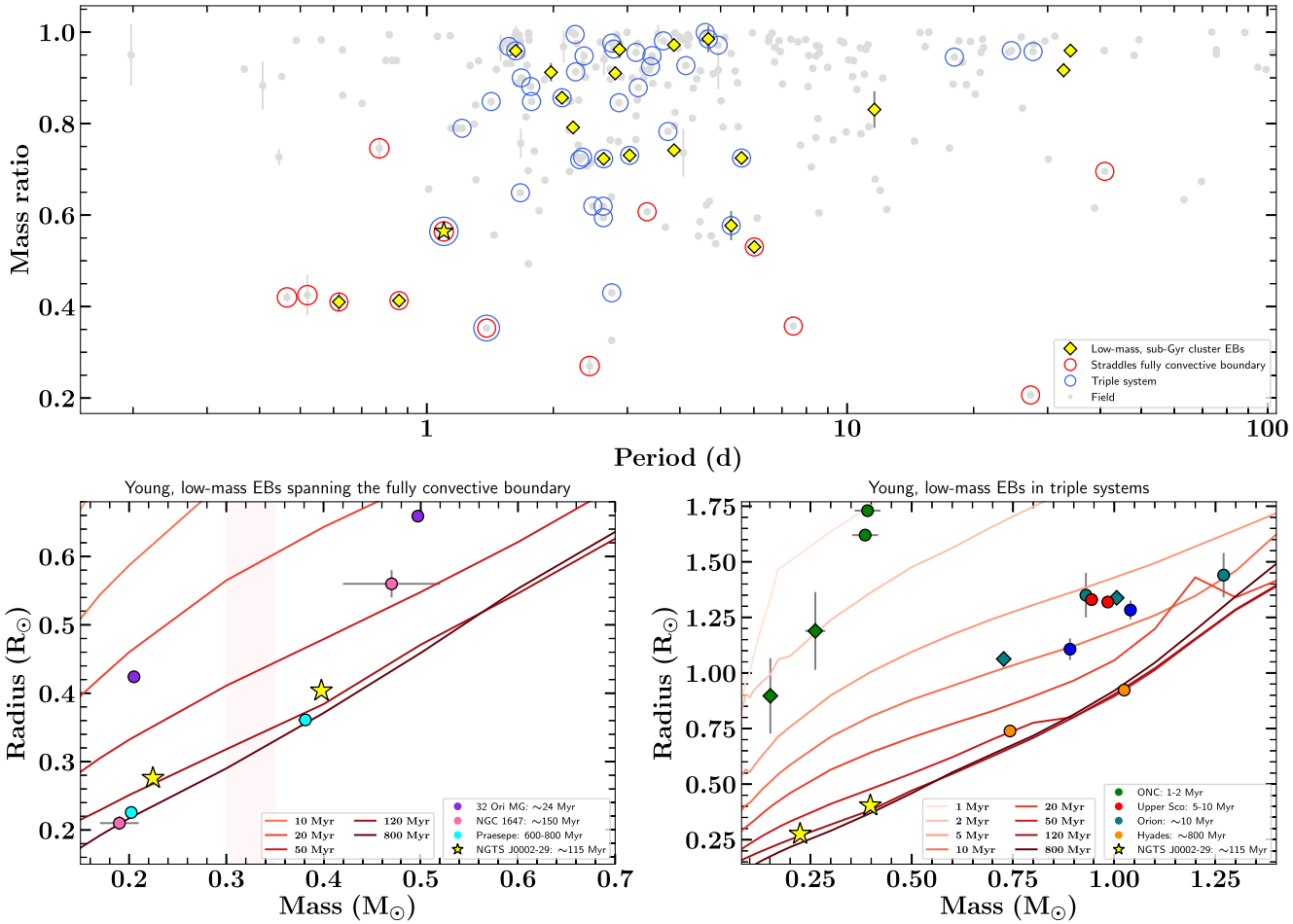

Figure 8. Top: Mass ratio versus orbital period for detached, double-lined, stellar-mass EBs. The well-characterized, low-mass, sub-Gyr-cluster systems collated by Gillen et al. (2017) and updated in Gillen et al. (2020a) are plotted with yellow diamonds. The field EBs from Irwin et al. (2009, 2018), Stassun et al. (2014), Nefs et al. (2013), Zhou et al. (2015), Dittmann et al. (2017), Casewell et al. (2018), Miller et al. (2021), and DEBCat (Southworth 2015) are plotted in grey. The red circles identify binaries where the components span the fully convective boundary, and the blue circles identify those with known tertiary companions. NGTS J0002−29 is shown with a yellow star. Bottom left: The four well-characterized, double-lined cluster EBs whose components span the fully convective boundary (pink vertical bar), along with BHAC15 isochrones from 10–800 Myr. Bottom right: The well-characterized, double-lined cluster EBs with component masses <1.5 M$_\odot$, which have known tertiary components, along with BHAC15 isochrones from 1–800 Myr.

binary period, with tertiary companions absent for the majority of binaries with $P > 6$ d. An obvious interpretation is that the tertiary companion plays a role in the creation of the closest binary systems. Current explanations of star formation preclude the *in situ* formation of close binaries, because the latter stages of collapse proceed from a hydrostatic core of radius ∼5 au, which is resistant to further fragmentation (Larson 1969; Bate 1998, 2011). The fragmentation of collapsing regions of cold molecular clouds may lead to bound binary or multiple stellar systems if multiple collapse events occur within a turbulent parent core (Offner et al. 2010; Kratter 2011). Alternatively, gravitational instability within a protostellar disc may lead to fragmentation and the birth of additional companions (Bonnell & Bate 1994; Kratter et al. 2010). In either of these scenarios of core or disc fragmentation, binary components separated by less than ∼10 au must have migrated inwards.

Recent population synthesis work by Moe & Kratter (2018) concluded that the majority of close binaries with $P < 10$ d form in the pre-main sequence (PMS), in agreement with observations, and derive from disc fragmentation followed by dynamical interactions of initially unstable triple systems, with significant energy dissipation in the disc, a mechanism consistent with the modelling of Tokovinin & Moe (2020). This is in contrast to orbital decay via Kozai–Lidov cycles and tidal friction in misaligned triples (e.g. Eggleton & Kisseleva-Eggleton 2006; Fabrycky & Tremaine 2007; Naoz & Fabrycky 2014).

Understanding the dynamic evolution of close binaries is of interest in the study of various astrophysical phenomena, e.g. binary mass exchange, mergers, and Type 1a supernovae, but also to the use of EBs as tests of stellar evolution theory. Stassun et al. (2014) showed how – for a sample of 13 benchmark PMS EBs – the stellar properties of systems with known tertiary companions were in much poorer agreement with the predictions of evolutionary models than those of lone binaries. They proposed that such discrepancies could be explained by the regular input of orbital energy from the tertiary to the binary, with tidal interactions between the binary components becoming significant if their separation was sufficiently reduced. The bottom-right plot in Fig. 8 shows isochrones from BHAC15, and the well-characterized, sub-Gyr, low-mass EBs with known tertiary companions. Despite a possibly inflated primary, NGTS J0002−29 is

one of the better fitted systems here. We also note that it is the shortest period EB with a known tertiary companion (see upper panel).

At the age of Blanco 1, M dwarfs are not expected to have quite settled on to the main sequence, though their radii will not reduce much further. The chaotic interactions and migration of early PMS life that may affect systems in the Stassun et al. (2014) sample, where ages span approximately 1–20 Myr, would not necessarily be a feature of NGTS J0002−29 at ∼115 Myr. Our modelling indicates that NGTS J0002−29 is circularized ($e \approx 0$). We also see OOE variability on (or very close to) the orbital period, suggesting synchronization, which, from theory, is expected to occur before circularization.[7] If NGTS J0002−29 is indeed circularized and synchronized, and if equatorial and orbital planes are aligned, then we expect tidal dissipation to be minimal with the binary in an equilibrium state (Hut 1981), unless the tertiary's orbit is small or eccentric enough to interfere.

Using the MCMC samples for the radius and effective temperature of the tertiary companion from our global modelling, we derive a tertiary mass of $M_{\rm ter} = 0.16 \pm 0.03$ M$_\odot$ from the BHAC15 stellar evolution models. This estimate was obtained by interpolating the models to compute a fine grid of the parameters (effective temperature and radius) at each mass, followed by a 2D cubic interpolation in $\log T_{\rm eff}$–R space (using the GRIDDATA routine in SCIPY) from our posterior distributions on to the grid, yielding a distribution of tertiary masses, from which we have quoted the median and 16th/84th percentiles. With this mass, the derived component luminosities, our measurements of the tertiary RVs, and the sensitivity of *Gaia*, we can attempt to put some loose constraints on the tertiary orbit. Given the derived luminosities of the tertiary and the binary, we would expect the tertiary to be resolved in *Gaia* for separations greater than ∼1 arcsec (Brandeker & Cataldi 2019), which implies that the tertiary is within ∼240 au of the binary. Given the scatter and uncertainties of our tertiary RVs, and the timing of our observations spanning 60 d, we estimate that we would only be sensitive to the reflex orbit of the tertiary if its separation is less than ∼1–2 au from the binary, assuming a co-planar, circular orbit. That we do not see variations indicative of such a close orbit leads to the conclusion that the tertiary is likely to orbit at a distance of ∼2–240 au. Additionally, we see no evidence for eclipse timing variations in our light curves; the eclipse minima are aligned with their predictions across the ∼1.5-yr baseline of photometric observations. This is consistent with the most likely scenario of a hierarchical triple, where the tertiary is distant and low mass.

5.2.3 *The fully convective boundary*

The transition into the fully convective regime for stellar interiors is predicted to occur at around 0.3–0.35 M$_\odot$ (Dorman, Nelson & Chau 1989; Chabrier & Baraffe 1997). Fully convective main-sequence stars are considered to be the simplest stars to describe theoretically, being relatively insensitive to model input parameters (Feiden & Chaboyer 2014b), but stellar evolution models frequently struggle to match observations for these, as well as higher mass, M dwarfs (e.g. Morales et al. 2009; Torres et al. 2010; Feiden & Chaboyer 2014b; Kesseli et al. 2018). Magnetic activity is often favoured as a potential cause of the disagreement between models and predictions, due to the inhibition of bulk convection or the creation of star-spots, but it is by no means resolved (Chabrier et al. 2007; Feiden & Chaboyer 2014a, b; Morrell & Naylor 2019).

In the past, some work has highlighted a possible difference in the amount of deviation from stellar evolution models above and below the fully convective boundary; for example, Morales et al. (2010) pointed to radii being much closer to theoretical models and less scattered for $M \lesssim 0.35$ M$_\odot$, with more scatter – but a larger deviation evident – for $M \gtrsim 0.35$ M$_\odot$. Recently, others have found no difference above and below the boundary (Parsons et al. 2018), while Kesseli et al. (2018), in their study of 88 rapidly rotating single M dwarf stars, found greater disparities between predicted and measured radii at the lowest masses (13–18 per cent for $0.08 < M < 0.18$ M$_\odot$ compared with 6 per cent for $0.18 < M < 0.4$ M$_\odot$), but also stated that there was no significant change in the amount of inflation compared to models *across* the fully convective boundary.

That there are different physics at play is less in doubt. When studying the effects of magnetic activity on low-mass stars, Chabrier et al. (2007) showed that fully convective stars are quite insensitive to changes in the mixing length parameter (which, when reduced, leads to decreased convective efficiency in partially convective stars), but that they are significantly affected by spot coverage. Within this framework, the measured properties of the most-studied – but highly discrepant – fully convective EB, CM Dra, may be reconcilable with suitably adjusted models (Morales et al. 2010). MacDonald & Mullan (2012) also fitted CM Dra to model predictions, but by invoking a magnetic inhibition parameter and suppression of convection, along with removing the effect of polar spots biasing radius values upwards in EB light-curve modelling. In both cases there is, however, much uncertainty, e.g. whether the large coverage of polar spots and/or the required supermegagauss magnetic fields actually exist (see Feiden & Chaboyer 2014b, for a detailed discussion).

It could be the case that the disagreement between models and observations has a different origin above and below the fully convective boundary due to the different physics involved, but there remains much to explain. Indeed, different physics does not necessarily manifest itself in all relations of interest. For example, despite the absence of a tachocline – the interface between radiative core and convective envelope, thought to be the location of magnetic field shearing and amplification in differentially rotating stars above the fully convective boundary (e.g. Charbonneau 2014) – lower mass stars have been found to follow an activity–rotation relation that is indistinguishable from their partially convective counterparts (Wright & Drake 2016; Wright et al. 2018).

In addition to similarities in some of the observed effects of their magnetic dynamos, fully convective stars are seen to fit the smooth trends in mass–luminosity and radius–luminosity through M spectral types (Demory et al. 2009). As noted by Stassun et al. (2011), it would appear that such stars are indifferent, in terms of energy generation and output, to changes in structure or energy transport within. However, in the mass–temperature and radius–temperature planes, the fully convective transition zone lies in a region of substantial change, where both theory and observation – albeit with an ∼250-K offset (e.g. Dupuy et al. 2010) – show there to be a large range of masses and radii for a small range of spectral types (Chabrier & Baraffe 2000; Stassun et al. 2011).

Narrowing the focus to open cluster EBs, there are, to our knowledge, only four well-characterized, double-lined, stellar-mass systems (NGTS J0002−29 included) that span the fully convective boundary (see Fig. 8, bottom left). These systems ought to be especially stringent tests of stellar evolution models because, as well as having well-determined parameters and ages, different physics are relevant to each component, plus the low mass ratios are good tests of

[7]Circularization and synchronization times are $t_{\rm circ} \approx 2$ Myr and $t_{\rm sync} \approx 0.03$ Myr by equations (6.2) and (6.1) in Zahn (1977), respectively, but we note that the theory therein is based on stars with convective envelopes.

model isochrone gradients. Interestingly, in these cases we have two systems – those in Praesepe (Gillen et al. 2017) and the 32 Orionis moving group (Murphy et al. 2020) – where the masses and radii of both components agree well with (non-magnetic) model predictions, and another two systems – in Blanco 1 (this work) and NGC 1647 (Hebb et al. 2006) – where it is the higher mass component that appears to be inflated (although the secondary in NGC 647 is smaller than expected for its assumed cluster age of 150 Myr). Three out of these four systems (not Praesepe) also have very short periods (∼1 d), meaning that they will be fast rotators (assuming spin–orbit synchronization) and hence would be expected to exhibit enhanced magnetic activity. That their lowest mass components do not appear to be inflated may be a clue that rotation-induced magnetic activity is not the explanation, or at least not the whole story, for those fully convective stars that appear inflated compared with models. With observations of fully convective stars that do and do not fit model radius predictions, the situation for stellar evolution modelling remains complex. It should be noted that models in all of the above four systems fail to predict the inferred temperatures of one or both components.

5.3 Comparison with stellar evolution models

We compare the fundamental parameters of NGTS J0002−29 with the closest-to-cluster-metallicity predictions of the following stellar evolution models in the mass–radius and $T_{\rm eff}$–log L planes (MRD and HRD hereafter): BHAC15; MESA Isochrones and Stellar Tracks (MIST v1.2, with $v/v_{\rm crit} = 0.4$[8]; Choi et al. 2016; Dotter 2016); PAdova and TRieste Stellar Evolution Code (PARSEC v.1.2S; Bressan et al. 2012); the standard and magnetic models of Feiden (Feiden 2016); and Stellar Parameters of Tracks with Starspots (SPOTS; Somers & Pinsonneault 2015; Somers, Cao & Pinsonneault 2020).

The BHAC15 models are an update to the models of Baraffe et al. (1998), now using BT-Settl model atmospheres and updated surface boundary conditions. The MIST v1.2 models are based on the MESA (Modules for Experiments in Stellar Astrophysics) stellar evolution package. Version 1.2S of the PARSEC models updates the relation between the temperature and Rosseland mean optical depth (T–τ) for the outer boundary conditions to that from the BT-Settl model atmospheres. Also included in v1.2S is a shift in the T–τ relations to reproduce the observed mass–radius relation of low-mass dwarf stars (Chen et al. 2014). We note that this shift means that the v1.2S models are not a direct test of the underlying stellar evolution theory.[9] The Feiden models are based on the Dartmouth Stellar Evolution Program (Dotter et al. 2008), and were further developed in Feiden & Chaboyer (2012b, 2013) and Feiden (2016) to include the effect of magnetic fields. Magnetic fields act to inhibit convection and hence slow PMS contraction, which generally results in older age predictions compared to non-magnetic models. The SPOTS models use the Yale Rotating Evolution Code and incorporate the structural effects of star-spots. The effects of spots in these models are to suppress the rate of convective energy transport in the stellar interior and to alter the average pressure and temperature at the model photosphere. The SPOTS models are divided into two zones: spotted and unspotted, each with an associated temperature at a given layer. The model temperature at any given radius within the star is then determined by summing the fluxes of the spotted and unspotted regions. Model isochrones are available for six different spot surface covering fractions; our comparisons use $f = 0$ per cent and $f = 17$ per cent.

In Fig. 9, we compare the properties of NGTS J0002−29 to the stellar evolution models described above. In each panel, the coloured lines represent five isochrones from 50 to 200 Myr, and the location of NGTS J0002−29 is shown with orange crosses. The grey dashed lines are evolutionary tracks at constant luminosity (in the MRD) and constant mass (in the HRD) for the values we have derived. In the HRD, we also plot (with black crosses) the location of NGTS J0002−29 as determined when using the PHOENIX (see Section 5.7), rather than BT-Settl model atmospheres. Table 6 compares model-predicted ages from the MRD and HRD. These estimates were arrived at by an equivalent procedure to that described in Section 5.2.2 for the derivation of the tertiary mass, but in this case we used model isochrones rather than evolutionary tracks. We interpolated the models to compute a fine grid of masses, radii, effective temperatures, and luminosities at each age, using isochrones at 20, 30, 40, 50, 80, 100, 120, and 200 Myr – a sampling density based on the finest available to all models. This was followed by a 2D cubic interpolation[10] from our posterior distributions on to the grid, to yield a distribution of ages. We do not give HRD age estimates based on the PARSEC models, because nearly all the data points fall well beyond the zero-age main sequence.

We find that the binary components appear coeval (within the 1σ error bars) in the MRD for the magnetic Feiden and PARSEC models, but component ages do not agree for any model in the HRD. There is greater uncertainty in the ages derived from the HRD than the MRD, which is a consequence of the measured masses and radii being better constrained than the effective temperatures and luminosities. It is evident from Table 6 that, with the exception of the secondary in the SPOTS 17 models, age predictions based on the HRD are systematically younger than those based on the MRD, with the discrepancy being greater for the primary. The primary ages are also younger than the secondary ages in both the MRD and HRD. This could be interpreted as the primary, rather than the fully convective secondary, being subject to inflation. The magnetic Feiden and SPOTS 17 models, as expected, produce older age estimates than the other models (PARSEC excluded), all of which are non-magnetic. They are also the only models whose MRD age predictions are consistent with the LDB age of 115 ± 10 Myr. In the HRD, the predicted age of the secondary for the magnetic Feiden models and the primary for the SPOTS 17 models are consistent with the LDB age. The primary and secondary ages between MRD and HRD are both consistent within the uncertainties for SPOTS 17, whereas it is only the secondary ages that are consistent for the magnetic Feiden models. One can see, when comparing the magnetic Feiden models and SPOTS 17 models in Fig. 9, that the posterior distributions lie in almost identical positions in the MRD, while appearing older for SPOTS 17 in the HRD. It is interesting to see how current magnetic stellar evolution models differ in their predictions, while bearing in mind that the Feiden models focus on how magnetic activity affects bulk convection, as opposed to the impact of star-spots. We note that we do not account for spots explicitly in the GP-EBOP model.

We can also look at the plotted evolutionary tracks and observe whether our derived luminosities (in the MRD) and masses (in the HRD) are consistent with model predictions. In the MRD, no models

[8]We have used the rotating set of MIST isochrones but note that these are equivalent to the non-rotating versions on the PMS.

[9]We include the PARSEC v1.2 models as they are commonly used in the literature and give quite different predictions to other models in the region of parameter space relevant to this work.

[10]We find that the 2D interpolation works best in log $T_{\rm eff}$–log L space for the HRD.

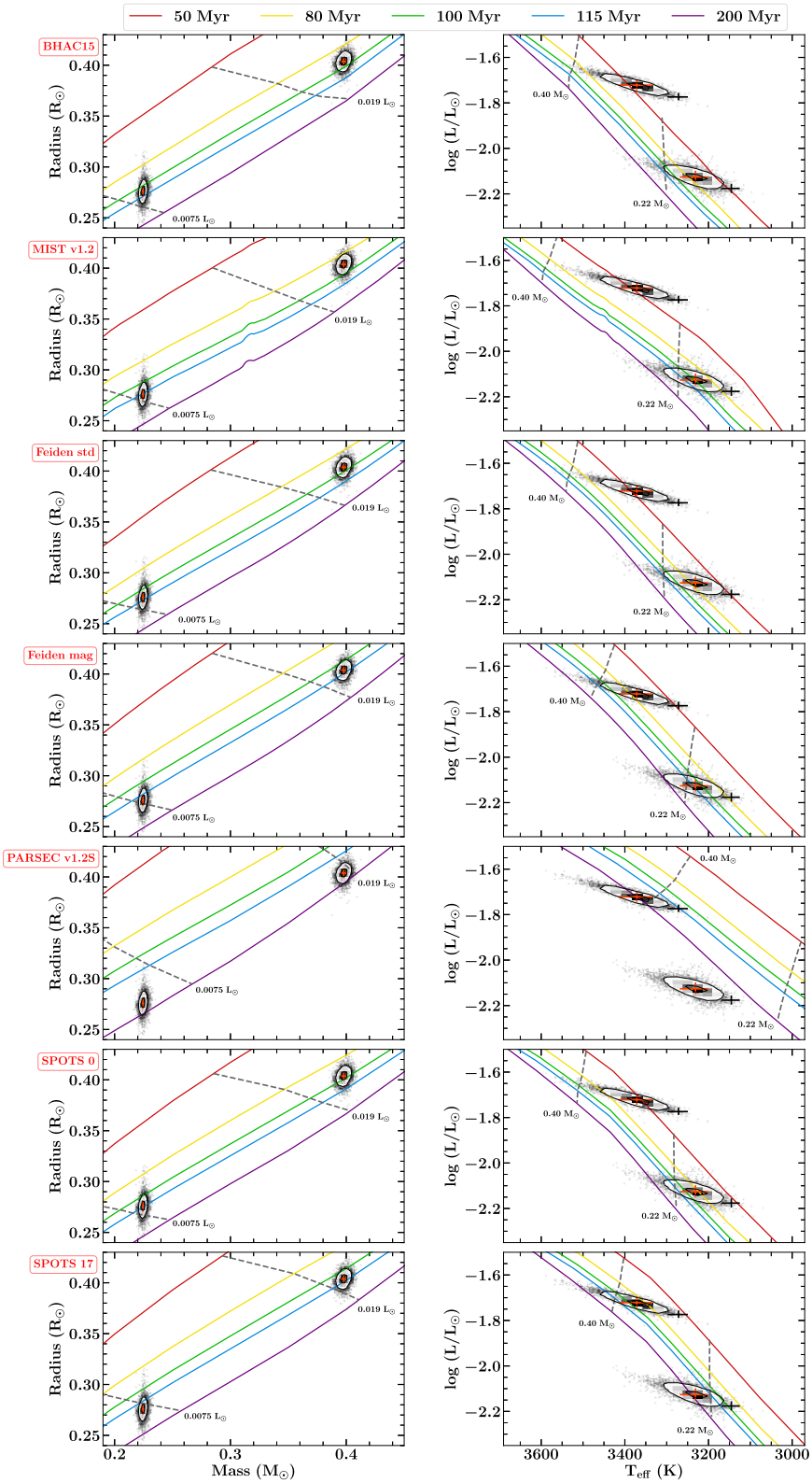

Figure 9. Comparison of the fundamental properties of NGTS J0002−29 to the predictions of the BHAC15, MIST v.1.2, Feiden std, Feiden mag, PARSEC v1.2S, SPOTS 0, and SPOTS 17 stellar evolution models in the mass–radius and $T_{\rm eff}$–log L planes. Isochrones at 50 (red), 80 (yellow), 100 (green), 115 (blue), and 200 (purple) Myr are plotted, along with isolumes (mass–radius plane) and evolutionary tracks ($T_{\rm eff}$–log L plane) as grey dashed lines. The median and 1σ bars from our posterior distributions are shown by orange crosses. The full distributions (grey dots), and the 1σ and 2σ contours of the 2D distributions (39 per cent and 86 per cent of the volume) are plotted using the contour function in CORNER (Foreman-Mackey 2016). Note that for the asymmetric distributions (in this case $T_{\rm eff}$ and log L), the 1D error bars do not align with the 2D 1σ contours. We also illustrate the effect of using PHOENIX model atmospheres by plotting black crosses in the $T_{\rm eff}$–log L plane. The masses and radii derived using the PHOENIX models are almost identical to the main results and so are not shown in the mass–radius plane.

Table 6. Isochronal ages of NGTS J0002−29 in the mass–radius (MR) and Hertzsprung–Russell (HR) diagrams.

Model	MRD age (Myr)		HRD age (Myr)	
	Primary	Secondary	Primary	Secondary
BHAC15	95 ± 4	106^{+8}_{-6}	44^{+10}_{-7}	71^{+17}_{-12}
MIST v1.2	90 ± 5	114^{+10}_{-7}	47^{+6}_{-5}	100^{+16}_{-13}
Feiden (std)	96^{+5}_{-4}	110^{+9}_{-6}	46^{+10}_{-8}	74^{+16}_{-12}
Feiden (mag)	109^{+7}_{-5}	124^{+12}_{-8}	73^{+17}_{-11}	110^{+31}_{-15}
PARSEC v1.2S	166^{+17}_{-15}	176^{+12}_{-11}	–	–
SPOTS 0	97 ± 4	112^{+9}_{-7}	54^{+12}_{-9}	85^{+20}_{-15}
SPOTS 17	109^{+7}_{-5}	127^{+13}_{-9}	90^{+15}_{-14}	179^{+57}_{-50}

give a good match to both components, although SPOTS 17 comes closest. The isolumes, in most cases, intersect the distributions for the secondary between the 1σ and 2σ regions, but not for the primary. In the HRD, the evolutionary tracks for the secondary are, again, reasonably well matched to our observations, with the magnetic models (Feiden mag in particular) doing the best. However, all models (except PARSEC) underpredict the primary mass. This highlights how the estimation of stellar masses for young, low-mass objects from model isochrones and observational HR diagrams can be problematic. Overall, we find that the predictions of the magnetic models (Feiden mag and SPOTS 17) are a better match to our measurements than those of the non-magnetic models.

5.4 Activity

There are X-ray observations of NGTS J0002−29 in the literature by *ROSAT* (Micela et al. 1999) and *XMM-Newton* (Pillitteri et al. 2003, 2004, 2005), in which the system is referred to either by its 2MASS ID or the designation BLX 24. The X-ray properties of the system, as given in Pillitteri et al. (2004), are log flux $= -13.68$ erg s^{-1} cm^{-2}; log $L_{\rm X} = 29.20$ erg s^{-1}; and $\log \frac{L_{\rm X}}{L_{\rm bol}} = -2.31$. It is found to be an X-ray variable in Pillitteri et al. (2005), although they note that its proximity to a chip gap and to another faint source might have influenced the evaluation of variability and the light curve.

In our HIRES spectrum, we see Hα and Hβ emission, and filled-in absorption features of the Ca II infrared triplet (8498/8542/8662 Å), indicative of magnetic activity. We do not see any evidence of lithium at 6708 Å in the HIRES or UVES spectra, but it is not expected for mid M dwarfs in Blanco 1 (Juarez et al. 2014). We fit the Hα emission profiles using the same method as applied to the BFs in Section 3.1, but with three Voigt functions in place of Gaussians. We measure equivalent widths of EW$_{\rm pri}$(H$\alpha \approx -4$ Å) and EW$_{\rm sec}$(H$\alpha \approx -1$ Å), but note that the three peaks are close in velocity space and so blending is an issue. We estimate measurement uncertainties of 5–10 per cent for the EWs, based on the values obtained in MCMC runs with different constraints.

In order to compare Hα emission between stars of different intrinsic luminosities, it is common to use the $L_{\rm H\alpha}/L_{\rm bol}$ metric (e.g. Walkowicz, Hawley & West 2004; Douglas et al. 2014; Newton et al. 2017). This is defined as $L_{\rm H\alpha}/L_{\rm bol} = {\rm EW}_{\rm H\alpha} \times f_0/{\rm f_{bol}}$, where f_0 is the continuum flux for the line. $f_0/f_{\rm bol}$ (χ hereafter) can be calculated either from high-quality data and bolometric corrections or from model atmospheres (Reiners & Basri 2007; Stassun et al. 2012; Douglas et al. 2014). Using BT-Settl model atmospheres and $T_{\rm eff}$, log g, and metallicity values closest to the binary components, and taking the continuum flux to be the mean flux between 6550–6560 and 6570–6580 Å, we calculate $\log \frac{L_{\rm H\alpha}}{L_{\rm bol}} = -3.81 \pm 0.03$ and -4.87 ± 0.03 for primary and secondary, respectively. Douglas et al. (2014) provide empirical spectral-type–χ relations and PHOENIX model $T_{\rm eff}$–χ relations, from which we find similar (though marginally larger) values. From the Hα indicator, it appears that the primary is more active than the secondary, which could explain its apparently greater inflation. This is, however, based on a single epoch, with blended emission peaks, so additional spectra (ideally closer to quadrature) would be desirable.

Stassun et al. (2012) give empirical relations for predicting the amount by which the effective temperatures and radii of low-mass stars are changed due to chromospheric activity. They base the relations on a large set of low-mass field stars with Hα measurements and a smaller set of low-mass EBs with X-ray activity measurements, from which they infer Hα activity. Using our calculated $L_{\rm H\alpha}/L_{\rm bol}$ values, the relations give $\Delta T_{\rm eff,pri} = -5 \pm 1$ per cent, $\Delta T_{\rm eff,sec} = -2 \pm 1$ per cent, $\Delta R_{\rm pri} = 10 \pm 1$ per cent and $\Delta R_{\rm sec} = -2 \pm 2$ per cent.[11] For the non-magnetic models, the primary does not appear inflated by as much as 10 per cent in the MRD, unless the system age is ∼200 Myr. Rather, the average inflation factor we observe at the nominal system age of ∼115 Myr is ∼4 per cent. However, we do see an uninflated secondary, in agreement with the empirical relations. Finally, shifting the primary by $\Delta T_{\rm eff} \sim 170$ K (∼5 per cent) and the secondary by $\Delta T_{\rm eff} \sim 65$ K (∼2 per cent) in the HRD would bring them into reasonable agreement with most non-magnetic models at ∼115 Myr. It should be noted that there is significant scatter in the Stassun et al. (2012) relations.

5.5 Age of NGTS J0002−29

As stated in Section 1, a number of age estimates have been made for Blanco 1 over the past ∼25 yr: 90 ± 25 Myr based on Hα emission (Panagi & O'dell 1997); LDB ages of 132 ± 24 and 115 ± 10 Myr (Cargile et al. 2010; Juarez et al. 2014); 146 ± 14 Myr based on gyrochronology (Cargile et al. 2014); and ∼100 Myr based on isochrone fitting (Z20). Z20 point out that the LDB age, adopted in G18 following a good fit to the lower main sequence, ought to be revisited. In the age of *Gaia*, there is good reason for such a study, because, out of the 14 stars taken to be Blanco 1 members in Juarez et al. (2014), only 3 (all bright objects) appear in the G18 and Z20 Blanco 1 member lists. The majority of stars in the LDB study are of course faint, making the confirmation of cluster membership more difficult, which is hence a possible reason for them being filtered out in G18 and Z20. Another reason could be that they are binaries and have high astrometric jitter. Table 6 shows the isochronal ages we derive for NGTS J0002−29 from the MRD and HRD. With the exception of the higher-than-expected PARSEC ages, we find MRD ages of ∼90–115 Myr from non-magnetic models and ∼110–125 Myr from magnetic models. HRD ages typically appear younger by ∼15–50 Myr.

5.6 Distance to NGTS J0002−29

G18 determined the parallax of the Blanco 1 cluster centre to be 4.216 ± 0.003 mas, equivalent to a distance of 237.19 ± 0.17 pc. Bailer-Jones et al. (2018) caution against directly converting parallaxes of individual objects into distances for those stars – a large majority in *Gaia* – where the relative uncertainty on the parallax is greater than 10–20 per cent. The formal relative uncertainty on the

[11] Radius deflation factors are probably unphysical. Stassun et al. (2012) say that offsets should simply approach zero at very low activity levels.

NGTS J0002−29 parallax in both DR2 and eDR3 is ∼7 per cent, but this is very large compared to stars of similar brightness and on-sky position, and is likely underestimated (El-Badry, Rix & Heintz 2021). There is also a large difference between the catalogue parallaxes, 3.9730 ± 0.2615 mas (252 ± 17 pc; DR2) and 3.7976 ± 0.2555 mas (263 ± 18 pc; eDR3),[12] and the G18 parallax of 4.616 ± 0.149 mas (217 ± 7 pc). The G18 parallax accounts for the measured proper motion, the parallax and space motion of the cluster centre, and the position of the star on the sky relative to the projection of the cluster centre (see also Gaia Collaboration 2017). Such 'kinematically improved' parallaxes are refinements for the vast majority of cluster members, but the fact that NGTS J0002−29 is a multistar system is problematic. Indeed, the *Gaia* astrometry is undoubtedly perturbed, as is evidenced by large error bars on the astrometric parameters and a large re-normalized unit weight error (RUWE = 4.15), the recommended statistical indicator for the reliability and quality of *Gaia* astrometry (Lindegren 2018). In the light of the work of Belokurov et al. (2020) and Stassun & Torres (2021), it is clear that the tertiary is the most likely cause of the astrometric perturbations.

We determine a distance to NGTS J0002−29 of 228 ± 6 pc. This result comes out of our global modelling, where the SED model fluxes are scaled by the solid angle subtended by the stars at the fitted distance. We placed a Jeffreys prior on the parallax over a range of 3–6 mas, initialized at the G18 value for the cluster centre.

5.7 Differences between using BT-Settl and PHOENIX atmosphere models

In order to test the effect of the stellar atmosphere model used, we also modelled the system using PHOENIX model atmospheres. The results from this run yielded almost identical masses and radii (and uncertainties) to those obtained using the BT-Settl model atmospheres, but with effective temperatures that were ∼90 K cooler, differing by $\sim 1.5\sigma$. The corresponding distance derived was smaller by ∼15 pc. Similar differences between these PHOENIX and BT-Settl model atmospheres have also been found in other studies of young, low-mass EBs; for example, Murphy et al. (2020) found that the PHOENIX models gave effective temperatures that were ∼30 K cooler in their study of an ∼24-Myr-old system, while Gillen et al. (2020a) found temperatures to be cooler by ∼160 and ∼125 K for the two <10-Myr-old systems analysed therein. The effect of the lower temperatures and luminosities in the context of stellar evolution models is illustrated in Fig. 9, where the black crosses in the HRDs are shifted down and to the right, relative to the main results. This shift corresponds to age predictions being between 11 and 85 Myr younger for the primary and between 23 and 84 Myr younger for the secondary.

5.8 Another EB in Blanco 1?

NGTS J0002−29 is the first well-characterized, low-mass EB in Blanco 1, but there exists a high-mass system that could also be a cluster member. The bright, early-type (B7V + B9V), double-lined EB, HD 224113 (*Gaia* eDR3 ID: 2314213698611350144), was characterized by Haefner, Skillen & de Groot (1987). Its *Gaia* parallax is consistent with Blanco 1, and despite a large range of recorded centre-of-mass velocities (ranging between −2.6 and +10.4 km s^{-1}), these would not rule out cluster membership. It is not listed as a member in G18 or Z20, but perturbed astrometry (RUWE = 2.50) is a plausible reason for its absence. Its on-sky position would place it as a moderate outlier among the G18 cluster members, although not an outlier within the proposed Z20 list. However, its proper motion, as measured by *Gaia* DR2/eDR3, would make it a more extreme outlier, compared with the *Gaia* DR2-confirmed members. Thus, to the best of our knowledge, the current census of EBs in Blanco 1 consists of either one or two systems, with NGTS J0002−29 potentially the only well-characterized EB in the cluster.

[12]Catalogue parallaxes are also subject to a small zero-point offset. The provisional correction function in Lindegren et al. (2020) suggests that the eDR3 parallax of NGTS J0002−29 is too small by ∼0.043 mas.

6 CONCLUSIONS

We have presented the identification and characterization of NGTS J0002−29 as an EB in the ∼115-Myr-old Blanco 1 open cluster. The star system is an M-dwarf triple, consisting of a detached, double-lined EB, whose components span the fully convective boundary, and a low-mass tertiary companion.

We simultaneously modelled light curves, RVs, and the system SED with GP-EBOP to yield high-precision parameter estimates, including masses to <1 per cent and radii to <2 per cent. We applied light ratio constraints from our UVES spectra, propagated through the SED model into the light-curve bands and hence into the eclipse modelling, in order to break the degeneracy between radius ratio, inclination, and surface brightness ratio. The data set was composed of our NGTS discovery light curve, *TESS* observations, follow-up photometry from SPECULOOS and SAAO, and spectra from VLT/UVES and Keck/HIRES.

We found that the binary components travel on circular orbits around their common centre of mass in $P_{\rm orb}$ = 1.098 005 24 ± 0.000 000 38 d, and have masses $M_{\rm pri}$ = 0.3978 ± 0.0033 $M_\odot$ and $M_{\rm sec}$ = 0.2245 ± 0.0018 $M_\odot$, radii $R_{\rm pri}$ = 0.4037 ± 0.0048 $R_\odot$ and $R_{\rm sec}$ = 0.2759 ± 0.0055 $R_\odot$, and effective temperatures $T_{\rm pri} = 3372^{+44}_{-37}$ K and $T_{\rm sec} = 3231^{+38}_{-31}$ K. We compared these properties to the predictions of seven stellar evolution models, revealing a possibly inflated primary. We found MRD ages of ∼90–115 Myr from non-magnetic models and ∼110–125 Myr from magnetic models.

NGTS J0002−29 is currently the only well-characterized EB of known age that has both a confirmed tertiary companion and components that straddle the fully convective boundary. Furthermore, it is one of only two well-characterized, low-mass EBs with an age close to ∼115 Myr, which makes the system a benchmark addition to the growing list of low-mass, sub-Gyr EBs that constitute some of the strongest observational tests of present and future stellar evolution theory at low masses and young ages.

ACKNOWLEDGEMENTS

This research is based on data collected under the NGTS project at the ESO La Silla Paranal Observatory. The NGTS facility is funded by a consortium of institutes consisting of the University of Warwick, the University of Leicester, Queen's University Belfast, the University of Geneva, the Deutsches Zentrum für Luft- und Raumfahrt e.V. (DLR; under the 'Großinvestition GI-NGTS'), and the University of Cambridge, together with the UK Science and Technology Facilities Council (STFC; project reference ST/M001962/1). This work is also based on observations collected at the European Southern Observatory under ESO programme 0103.C-0902(A) and at the W. M. Keck Observatory, which is operated as a scientific partnership among the California Institute of Technology, the University of

California, and the National Aeronautics and Space Administration. This research received funding from the European Research Council (ERC) under the European Union's Horizon 2020 research and innovation programme (grant agreement number 803193/BEBOP), and from the Science and Technology Facilities Council (STFC; grant numbers ST/S00193X/1 and ST/S00305/1).

GDS gratefully acknowledges support by an STFC-funded PhD studentship and thanks Simon Hodgkin and Floor van Leeuwen for helpful discussion concerning the *Gaia* astrometry. EG gratefully acknowledges support from the David and Claudia Harding Foundation in the form of a Winton Exoplanet Fellowship. MNG acknowledges support from MIT's Kavli Institute as a Juan Carlos Torres Fellow. LD is an F.R.S.-FNRS Postdoctoral Researcher. Finally, we would like to thank the referee, John Southworth, for his helpful and very positive report.

DATA AVAILABILITY

The data underlying this article will be shared on reasonable request to the corresponding author.

NOTE ADDED IN PROOF

After acceptance, we became aware of an additional publicly available light curve for the system from *TESS* Cycle 3. Including this data does not change the fundamental stellar parameters, and hence the paper's results and conclusions are unaltered.

REFERENCES

Acton J. S. et al., 2020a, MNRAS, 494, 3950
Acton J. S. et al., 2020b, MNRAS, 498, 3115
Ahmed S., Warren S. J., 2019, A&A, 623, A127
Allard F., Homeier D., Freytag B., 2012, Phil. Trans. R. Soc. London Ser. A, 370, 2765
Ambikasaran S., Foreman-Mackey D., Greengard L., Hogg D. W., O'Neil M., 2015, IEEE Trans. Pattern Anal. Mach. Intell., 38, 252
Andersen J., 1991, A&AR, 3, 91
Astropy Collaboration, 2013, A&A, 558, A33
Astropy Collaboration, 2018, AJ, 156, 123
Bailer-Jones C. A. L., Rybizki J., Fouesneau M., Mantelet G., Andrae R., 2018, AJ, 156, 58
Ballester P., Modigliani A., Boitquin O., Cristiani S., Hanuschik R., Kaufer A., Wolf S., 2000, The Messenger, 101, 31
Baraffe I., Chabrier G., Allard F., Hauschildt P. H., 1998, A&A, 337, 403
Baraffe I., Homeier D., Allard F., Chabrier G., 2015, A&A, 577, A42
Barbary K., 2016, J. Open Source Softw., 1, 58
Barnes J. R., 2004, MNRAS, 348, 1295
Bastian N., Covey K. R., Meyer M. R., 2010, ARA&A, 48, 339
Bate M. R., 1998, ApJ, 508, L95
Bate M. R., 2000, MNRAS, 314, 33
Bate M. R., 2011, MNRAS, 417, 2036
Bate M. R., Bonnell I. A., 1997, MNRAS, 285, 33
Bate M. R., Bonnell I. A., Bromm V., 2002, MNRAS, 336, 705
Bayliss D. et al., 2018, MNRAS, 475, 4467
Bell C. P. M., Naylor T., Mayne N. J., Jeffries R. D., Littlefair S. P., 2013, MNRAS, 434, 806
Belokurov V. et al., 2020, MNRAS, 496, 1922
Berger T. A., Huber D., Gaidos E., van Saders J. L., 2018, ApJ, 866, 99
Bergfors C. et al., 2010, A&A, 520, A54
Blanco V. M., 1949, PASP, 61, 183
Bonnell I. A., Bate M. R., 1994, MNRAS, 269, L45
Boyajian T. S. et al., 2012, ApJ, 757, 112
Brandeker A., Cataldi G., 2019, A&A, 621, A86
Bressan A., Marigo P., Girardi L., Salasnich B., Dal Cero C., Rubele S., Nanni A., 2012, MNRAS, 427, 127
Bryant E. M. et al., 2021, MNRAS, 504, L45
Burdanov A., Delrez L., Gillon M., Jehin E., 2018, in Deeg H., Belmonte J. A., eds, Handbook of Exoplanets. Springer Int. Publ. AG, Basel, p. 130
Burke C. J. et al., 2015, ApJ, 809, 8
Cargile P. A., James D. J., Jeffries R. D., 2010, ApJ, 725, L111
Cargile P. A., James D. J., Pepper J., Kuhn R. B., Siverd R., Stassun K. G., 2014, ApJ, 782, 29
Casewell S. L., Baker D. E. A., Jameson R. F., Hodgkin S. T., Dobbie P. D., Moraux E., 2012, MNRAS, 425, 3112
Casewell S. L. et al., 2018, MNRAS, 481, 1897
Chabrier G., Baraffe I., 1997, A&A, 327, 1039
Chabrier G., Baraffe I., 2000, ARA&A, 38, 337
Chabrier G., Gallardo J., Baraffe I., 2007, A&A, 472, L17
Chambers K. C. et al., 2016, preprint (arXiv:1612.05560)
Charbonneau P., 2014, ARA&A, 52, 251
Chazelas B. et al., 2012, in Stepp L. M., Gilmozzi R., Hall H. J., eds, Proc. SPIE Conf. Ser. Vol. 8444, Ground-Based and Airborne Telescopes IV. SPIE, Bellingham, p. 84440E
Chen Y., Girardi L., Bressan A., Marigo P., Barbieri M., Kong X., 2014, MNRAS, 444, 2525
Choi J., Dotter A., Conroy C., Cantiello M., Paxton B., Johnson B. D., 2016, ApJ, 823, 102
Chubak C., Marcy G., Fischer D. A., Howard A. W., Isaacson H., Johnson J. A., Wright J. T., 2012, preprint (arXiv:1207.6212)
Claret A., Bloemen S., 2011, A&A, 529, A75
Cohen M., Wheaton W. A., Megeath S. T., 2003, AJ, 126, 1090
Coppejans R. et al., 2013, PASP, 125, 976
Czesla S., Schröter S., Schneider C. P., Huber K. F., Pfeifer F., Andreasen D. T., Zechmeister M., 2019, Astrophysics Source Code Library, record ascl:1906.010
Dahm S. E., 2015, ApJ, 813, 108
David T. J. et al., 2016, AJ, 151, 112
David T. J., Hillenbrand L. A., Gillen E., Cody A. M., Howell S. B., Isaacson H. T., Livingston J. H., 2019, ApJ, 872, 161
de Val-Borro M., Gahm G. F., Stempels H. C., Pepliński A., 2011, MNRAS, 413, 2679
Dekker H., D'Odorico S., Kaufer A., Delabre B., Kotzlowski H., 2000, in Iye M., Moorwood A. F., eds, Proc. SPIE Conf. Ser. Vol. 4008, Optical and IR Telescope Instrumentation and Detectors. SPIE, Bellingham, p. 534
Delrez L. et al., 2018, in Marshall H. K., Spyromilio J., eds, Proc. SPIE Conf. Ser. Vol. 10700, Ground-Based and Airborne Telescopes VII. SPIE, Bellingham, p. 107001I
Demory B.-O. et al., 2009, A&A, 505, 205
Dittmann J. A. et al., 2017, ApJ, 836, 124
Dorman B., Nelson L. A., Chau W. Y., 1989, ApJ, 342, 1003
Dotter A., 2016, ApJS, 222, 8
Dotter A., Chaboyer B., Jevremović D., Kostov V., Baron E., Ferguson J. W., 2008, ApJS, 178, 89
Douglas S. T. et al., 2014, ApJ, 795, 161
Duchêne G., Kraus A., 2013, ARA&A, 51, 269
Dupuy T. J., Liu M. C., Bowler B. P., Cushing M. C., Helling C., Witte S., Hauschildt P., 2010, ApJ, 721, 1725
Eggleton P. P., Kisseleva-Eggleton L., 2006, Ap&SS, 304, 75
El-Badry K., Rix H.-W., Tian H., Duchêne G., Moe M., 2019, MNRAS, 489, 5822
El-Badry K., Rix H.-W., Heintz T. M., 2021, MNRAS, 506, 2269
Fabrycky D., Tremaine S., 2007, ApJ, 669, 1298
Feiden G. A., 2016, A&A, 593, A99
Feiden G. A., Chaboyer B., 2012a, ApJ, 757, 42
Feiden G. A., Chaboyer B., 2012b, ApJ, 761, 30
Feiden G. A., Chaboyer B., 2013, ApJ, 779, 183
Feiden G. A., Chaboyer B., 2014a, in Petit P., Jardine M., Spruit H. C., eds, Proc. IAU Symp. 302, Magnetic Fields throughout Stellar Evolution. Kluwer, Dordrecht, p. 150
Feiden G. A., Chaboyer B., 2014b, ApJ, 789, 53
Feinstein A. D. et al., 2019, PASP, 131, 094502

Fitzpatrick E. L., 1999, PASP, 111, 63
Ford A., Jeffries R. D., Smalley B., 2005, MNRAS, 364, 272
Foreman-Mackey D., 2016, J. Open Source Softw., 1, 24
Foreman-Mackey D., 2018, Res. Notes Am. Astron. Soc., 2, 31
Foreman-Mackey D., Hogg D. W., Lang D., Goodman J., 2013, PASP, 125, 306
Foreman-Mackey D., Agol E., Ambikasaran S., Angus R., 2017, AJ, 154, 220
Freudling W., Romaniello M., Bramich D. M., Ballester P., Forchi V., García-Dabló C. E., Moehler S., Neeser M. J., 2013, A&A, 559, A96
Gaia Collaboration, 2017, A&A, 601, A19
Gaia Collaboration, 2018, A&A, 616, A10 (G18)
Gaia Collaboration, 2020, A&A, 649, A1
Gaidos E., Mann A. W., 2013, ApJ, 762, 41
Gill S. et al., 2020, ApJ, 898, L11
Gillen E. et al., 2014, A&A, 562, A50
Gillen E., Hillenbrand L. A., David T. J., Aigrain S., Rebull L., Stauffer J., Cody A. M., Queloz D., 2017, ApJ, 849, 11
Gillen E., Hillenbrand L. A., Stauffer J., Aigrain S., Rebull L., Cody A. M., 2020a, MNRAS, 495, 1531
Gillen E. et al., 2020b, MNRAS, 492, 1008
Gillon M., 2018, Nat. Astron., 2, 344
Gómez Maqueo Chew Y. et al., 2019, A&A, 623, A23
Günther M. N. et al., 2017, MNRAS, 472, 295
Haefner R., Skillen I., de Groot M., 1987, A&A, 179, 141
Haisch K. E., Jr, Lada E. A., Lada C. J., 2001, ApJ, 553, L153
Hanawa T., Ochi Y., Ando K., 2009, ApJ, 708, 485
Hebb L., Wyse R. F. G., Gilmore G., Holtzman J., 2006, AJ, 131, 555
Henden A. A., 2019, J. Am. Assoc. Var. Star Obs., 47, 130
Henry T. J., Walkowicz L. M., Barto T. C., Golimowski D. A., 2002, AJ, 123, 2002
Hensberge H., Pavlovski K., 2007, in Hartkopf W. I., Harmanec P., Guinan E. F., eds, Proc. IAU Symp. 240, Binary Stars as Critical Tools & Tests in Contemporary Astrophysics. Cambridge Univ. Press, Cambridge, p. 136
Hillenbrand L. A., Bauermeister A., White R. J., 2008, in van Belle G., ed., ASP Conf. Ser. Vol. 384, 14th Cambridge Workshop on Cool Stars, Stellar Systems, and the Sun. Astron. Soc. Pac., San Francisco, p. 200
Husser T.-O., Wende-von Berg S., Dreizler S., Homeier D., Reiners A., Barman T., Hauschildt P. H., 2013, A&A, 553, A6
Hut P., 1981, A&A, 99, 126
Indebetouw R. et al., 2005, ApJ, 619, 931
Irwin J. et al., 2009, ApJ, 701, 1436
Irwin J. M. et al., 2011, ApJ, 742, 123
Irwin J. M. et al., 2018, AJ, 156, 140
Jackman J. A. G. et al., 2019, MNRAS, 489, 5146
Jackman J. A. G. et al., 2020, MNRAS, 497, 809
Jones A., Noll S., Kausch W., Szyszka C., Kimeswenger S., 2013, A&A, 560, A91
Juarez A. J., Cargile P. A., James D. J., Stassun K. G., 2014, ApJ, 795, 143
Karamanis M., Beutler F., Peacock J. A., 2021, preprint (arXiv:2105.03468)
Kesseli A. Y., Muirhead P. S., Mann A. W., Mace G., 2018, AJ, 155, 225
Kipping D. M., 2013, MNRAS, 435, 2152
Kovács G., Zucker S., Mazeh T., 2002, A&A, 391, 369
Kratter K. M., 2011, in Schmidtobreick L., Schreiber M. R., Tappert C., eds, ASP Conf. Ser. Vol. 447, Evolution of Compact Binaries. Astron. Soc. Pac., San Francisco, p. 47
Kratter K. M., Matzner C. D., Krumholz M. R., Klein R. I., 2010, ApJ, 708, 1585
Kraus A. L., Tucker R. A., Thompson M. I., Craine E. R., Hillenbrand L. A., 2011, ApJ, 728, 48
Laithwaite R. C., Warren S. J., 2020, MNRAS, 499, 2587
Laos S., Stassun K. G., Mathieu R. D., 2020, ApJ, 902, 107
Larson R. B., 1969, MNRAS, 145, 271
Lindegren L., 2018, Re-normalising the Astrometric Chi-Square in Gaia DR2, gAIA-C3-TN-LU-LL-124, available at http://www.rssd.esa.int/doc_fetch.php?id = 3757412
Lindegren L. et al., 2020, A&A, 649, A4
McCormac J. et al., 2017, PASP, 129, 025002
MacDonald J., Mullan D. J., 2012, MNRAS, 421, 3084
Mamajek E. E., Hillenbrand L. A., 2008, ApJ, 687, 1264
Mandel K., Agol E., 2002, ApJ, 580, L171
Mann A. W., Feiden G. A., Gaidos E., Boyajian T., von Braun K., 2015, ApJ, 804, 64
Maxted P. F. L. et al., 2020, MNRAS, 498, 332
Meibom S., Barnes S. A., Platais I., Gilliland R. L., Latham D. W., Mathieu R. D., 2015, Nature, 517, 589
Micela G., Sciortino S., Favata F., Pallavicini R., Pye J., 1999, A&A, 344, 83
Miller A., Kounkel M., Boggio C., Covey K., Price-Whelan A. M., 2021, PASP, 133, 044201
Moe M., Di Stefano R., 2017, ApJS, 230, 15
Moe M., Kratter K. M., 2018, ApJ, 854, 44
Moehler S. et al., 2014, The Messenger, 158, 16
Morales J. C. et al., 2009, ApJ, 691, 1400
Morales J. C., Gallardo J., Ribas I., Jordi C., Baraffe I., Chabrier G., 2010, ApJ, 718, 502
Moraux E., Bouvier J., Stauffer J. R., Barrado y Navascués D., Cuillandre J.-C., 2007, A&A, 471, 499
Morrell S., Naylor T., 2019, MNRAS, 489, 2615
Mullan D. J., MacDonald J., 2001, ApJ, 559, 353
Murphy S. J. et al., 2020, MNRAS, 491, 4902
Murray C. A. et al., 2020, MNRAS, 495, 2446
Naoz S., Fabrycky D. C., 2014, ApJ, 793, 137
Nefs S. V. et al., 2013, MNRAS, 431, 3240
Netopil M., Paunzen E., Heiter U., Soubiran C., 2016, A&A, 585, A150
Newton E. R., Irwin J., Charbonneau D., Berlind P., Calkins M. L., Mink J., 2017, ApJ, 834, 85
Nidever D. L., Marcy G. W., Butler R. P., Fischer D. A., Vogt S. S., 2002, ApJS, 141, 503
Noll S., Kausch W., Barden M., Jones A. M., Szyszka C., Kimeswenger S., Vinther J., 2012, A&A, 543, A92
Ochi Y., Sugimoto K., Hanawa T., 2005, ApJ, 623, 922
Offner S. S. R., Kratter K. M., Matzner C. D., Krumholz M. R., Klein R. I., 2010, ApJ, 725, 1485
Onken C. A. et al., 2019, Publ. Astron. Soc. Aust., 36, e033
Panagi P. M., O'dell M. A., 1997, A&AS, 121, 213
Parsons S. G. et al., 2018, MNRAS, 481, 1083
Parviainen H., Aigrain S., 2015, MNRAS, 453, 3821
Perruchot S. et al., 2008, in McLean I. S., Casali M. M., eds, Proc. SPIE Conf. Ser. Vol. 7014, Ground-Based and Airborne Instrumentation for Astronomy II. SPIE, Bellingham, p. 70140J
Pillitteri I., Micela G., Sciortino S., Favata F., 2003, A&A, 399, 919
Pillitteri I., Micela G., Sciortino S., Damiani F., Harnden F. R., 2004, A&A, 421, 175
Pillitteri I., Micela G., Reale F., Sciortino S., 2005, A&A, 430, 155
Raghavan D. et al., 2010, ApJS, 190, 1
Reiners A., Basri G., 2007, ApJ, 656, 1121
Ribas Á., Merín B., Bouy H., Maud L. T., 2014, A&A, 561, A54
Ribas Á., Bouy H., Merín B., 2015, A&A, 576, A52
Ricker G. R. et al., 2015, J. Astron. Telesc. Instrum. Syst., 1, 014003
Riello M. et al., 2021, A&A, 649, A3
Rix H.-W., White S. D. M., 1992, MNRAS, 254, 389
Rucinski S. M., 1992, AJ, 104, 1968
Rucinski S., 1999, in Hearnshaw J. B., Scarfe C. D., eds, ASP Conf. Ser. Vol. 185: Precise Stellar Radial Velocities. Astron. Soc. Pac., San Francisco, p. 82
Rucinski S. M., 2002, AJ, 124, 1746
Sebastian D. et al., 2021, A&A, 645, A100
Skrutskie M. F. et al., 2006, AJ, 131, 1163
Soderblom D. R., 2010, ARA&A, 48, 581
Soderblom D. R., Hillenbrand L. A., Jeffries R. D., Mamajek E. E., Naylor T., 2014, in Beuther H., Klessen R. S., Dullemond C. P., Henning T., eds, Protostars and Planets VI. Univ. Arizona Press, Tucson, AZ, p. 219
Somers G., Pinsonneault M. H., 2015, ApJ, 807, 174
Somers G., Cao L., Pinsonneault M. H., 2020, ApJ, 891, 29

Soubiran C. et al., 2018, A&A, 616, A7
Southworth J., 2015, in Rucinski S. M., Torres G., Zejda M., eds, ASP Conf. Ser. Vol. 496, Living Together: Planets, Host Stars and Binaries. Astron. Soc. Pac., San Francisco, p. 164
Southworth J., 2021, preprint (arXiv:2106.04323)
Spada F., Demarque P., Kim Y.-C., Sills A., 2013, ApJ, 776, 87
Stassun K. G., Torres G., 2021, ApJ, 907, L33
Stassun K. G. et al., 2011, in Johns-Krull C., Browning M. K., West A. A., eds, ASP Conf. Ser. Vol. 448, 16th Cambridge Workshop on Cool Stars, Stellar Systems, and the Sun. Astron. Soc. Pac., San Francisco, p. 505
Stassun K. G., Kratter K. M., Scholz A., Dupuy T. J., 2012, ApJ, 756, 47
Stassun K. G., Feiden G. A., Torres G., 2014, New Astron. Rev., 60, 1
Stauffer J. R., Schultz G., Kirkpatrick J. D., 1998, ApJ, 499, L199
Tamuz O., Mazeh T., Zucker S., 2005, MNRAS, 356, 1466
Tody D., 1986, in Crawford D. L., ed., Proc. SPIE Conf. Ser. Vol. 627, Instrumentation in Astronomy VI. SPIE, Bellingham, p. 733
Tokovinin A., Moe M., 2020, MNRAS, 491, 5158
Tokovinin A., Thomas S., Sterzik M., Udry S., 2006, A&A, 450, 681
Tonry J. L. et al., 2012, ApJ, 750, 99
Torres G., 2013, Astron. Nachr., 334, 4
Torres G., Andersen J., Giménez A., 2010, A&AR, 18, 67
Torres G., Curtis J. L., Vanderburg A., Kraus A. L., Rizzuto A., 2018, ApJ, 866, 67
Triaud A. H. M. J. et al., 2020, Nat. Astron., 4, 650
Trimble V., 1990, MNRAS, 242, 79
Vogt S. S. et al., 1994, in Crawford D. L., Craine E. R., eds, Proc. SPIE Conf. Ser. Vol. 2198, Instrumentation in Astronomy VIII. SPIE, Bellingham, p. 362
von Braun K. et al., 2012, ApJ, 753, 171
Walkowicz L. M., Hawley S. L., West A. A., 2004, PASP, 116, 1105
West R. G. et al., 2019, MNRAS, 486, 5094
Wheatley P. J. et al., 2013, in Saglia R., ed., Eur. Phys. J. Web Conf., Vol. 47, Hot Planets and Cool Stars. EDP Sci., Les Ulis Cedex A, p. 13002
Wheatley P. J. et al., 2017, MNRAS, 475, 4476
Windmiller G., Orosz J. A., Etzel P. B., 2010, ApJ, 712, 1003
Wright N. J., Drake J. J., 2016, Nature, 535, 526
Wright E. L. et al., 2010, AJ, 140, 1868
Wright N. J., Newton E. R., Williams P. K. G., Drake J. J., Yadav R. K., 2018, MNRAS, 479, 2351
Young M. D., Clarke C. J., 2015, MNRAS, 452, 3085
Zahn J.-P., 1977, A&A, 500, 121
Zhang Y., Tang S.-Y., Chen W. P., Pang X., Liu J. Z., 2020, ApJ, 889, 99 (Z20)
Zhou G. et al., 2015, MNRAS, 451, 2263

This paper has been typeset from a TEX/LATEX file prepared by the author.